# Interrogation of the Microenvironmental Landscape in Brain Tumors Reveals Disease-Specific Alterations of Immune Cells

Graphical Abstract
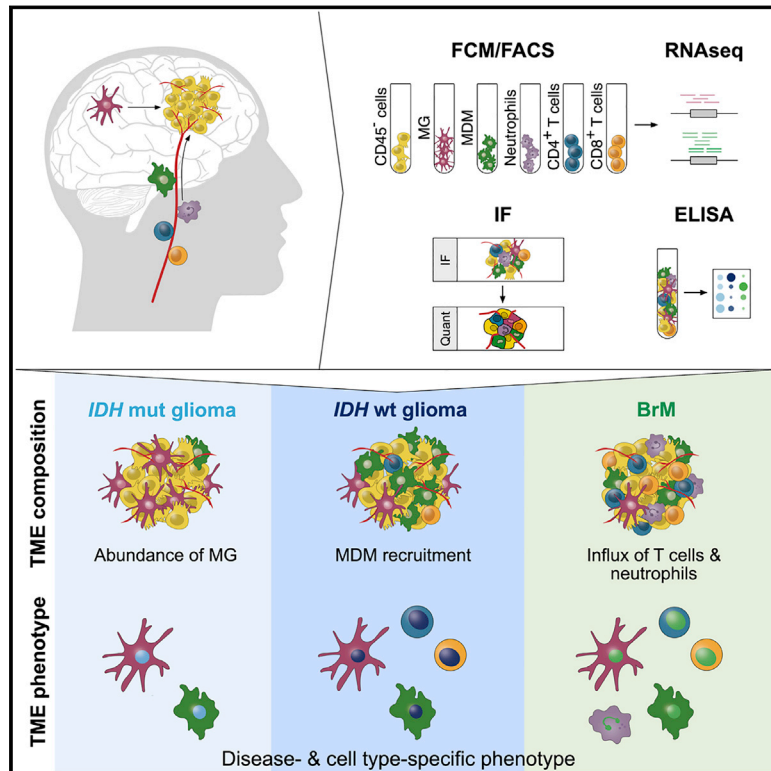
Authors

Florian Klemm, Roeltje R. Maas, Robert L. Bowman, ..., Roy T. Daniel, Monika E. Hegi, Johanna A. Joyce

Correspondence

johanna.joyce@unil.ch

In Brief

High-dimensional, multi-omics characterization of the brain tumor microenvironment, including comparisons of gliomas and brain metastases, suggests that education of immune cell types in the TME depends on tumor origin and *IDH* mutational status.

Highlights

- Flow cytometry, RNA-seq, and protein and image analyses reveal brain TME complexity

- Glioma *IDH* mutation status and brain metastasis primary tumors shape the brain TME

- Microglia and monocyte-derived macrophages exhibit multifaceted activation

- TME immune cells show disease- and cell-type-specific expression patterns

CellPress

Cell

CellPress

Resource

Interrogation of the Microenvironmental Landscape in Brain Tumors Reveals Disease-Specific Alterations of Immune Cells

Florian Klemm,[1,2] Roeltje R. Maas,[1,2,3,4] Robert L. Bowman,[5] Mara Kornete,[1,2] Klara Soukup,[1,2] Sina Nassiri,[1,2,6] Jean-Philippe Brouland,[7] Christine A. Iacobuzio-Donahue,[8] Cameron Brennan,[9] Viviane Tabar,[9] Philip H. Gutin,[9] Roy T. Daniel,[4] Monika E. Hegi,[3,4] and Johanna A. Joyce[1,2,10,*]

[1]Department of Oncology, University of Lausanne, Lausanne, Switzerland
[2]Ludwig Institute for Cancer Research, University of Lausanne, Lausanne, Switzerland
[3]Neuroscience Research Center, Centre Hospitalier Universitaire Vaudois, Lausanne, Switzerland
[4]Department of Neurosurgery, Centre Hospitalier Universitaire Vaudois, Lausanne, Switzerland
[5]Memorial Sloan Kettering Cancer Center, New York, NY, USA
[6]Bioinformatics Core Facility, SIB Swiss Institute of Bioinformatics, Lausanne, Switzerland
[7]Department of Pathology, Centre Hospitalier Universitaire Vaudois, Lausanne, Switzerland
[8]Department of Pathology, Memorial Sloan Kettering Cancer Center, New York, NY, USA
[9]Department of Neurosurgery, Memorial Sloan Kettering Cancer Center, New York, NY, USA
[10]Lead Contact
*Correspondence: johanna.joyce@unil.ch
https://doi.org/10.1016/j.cell.2020.05.007

SUMMARY

Brain malignancies encompass a range of primary and metastatic cancers, including low-grade and high-grade gliomas and brain metastases (BrMs) originating from diverse extracranial tumors. Our understanding of the brain tumor microenvironment (TME) remains limited, and it is unknown whether it is sculpted differentially by primary versus metastatic disease. We therefore comprehensively analyzed the brain TME landscape via flow cytometry, RNA sequencing, protein arrays, culture assays, and spatial tissue characterization. This revealed disease-specific enrichment of immune cells with pronounced differences in proportional abundance of tissue-resident microglia, infiltrating monocyte-derived macrophages, neutrophils, and T cells. These integrated analyses also uncovered multifaceted immune cell activation within brain malignancies entailing converging transcriptional trajectories while maintaining disease- and cell-type-specific programs. Given the interest in developing TME-targeted therapies for brain malignancies, this comprehensive resource of the immune landscape offers insights into possible strategies to overcome tumor-supporting TME properties and instead harness the TME to fight cancer.

INTRODUCTION

Brain malignancies include tumors that arise within the brain, such as low-grade gliomas and glioblastomas, and brain metastases (BrMs), which originate from extracranial primary tumors, including melanoma, breast, and lung cancers (Cagney et al., 2017). Gliomas mutant for the metabolic enzymes isocitrate dehydrogenase 1 and 2 (*IDH* mut) are generally low grade (II or III) and have a significantly better prognosis than *IDH* wild-type (WT) tumors, which are typically grade IV glioblastomas. Despite standard of care treatment comprising surgery followed by radiation and temozolomide (Stupp et al., 2005), median survival rates for glioblastoma patients remain stubbornly low (Aldape et al., 2019). Patient survival following BrM diagnosis can be even lower, with rates typically measured in months (Cagney et al., 2017; Ceccarelli et al., 2016), and among all adult brain tu-

mors, the incidence of BrMs significantly exceeds that of gliomas.

Given the current limited treatment options for these patients, a key question to address is whether a deep comprehensive understanding of how primary and metastatic cancers develop within the brain tumor microenvironment (TME) could reveal promising new targets for therapeutic intervention. Although diverse TME cell types can critically regulate cancer progression and response to therapy across a broad range of extracranial tumors (Klemm and Joyce, 2015), we cannot simply extrapolate findings from these cancers to the singular brain TME, given its unique cell types, including astrocytes, neurons, and microglia (MG); the immune-suppressive environment of this organ; and the challenges presented for cells and drugs to cross the blood-brain barrier (BBB) (Quail and Joyce, 2017).
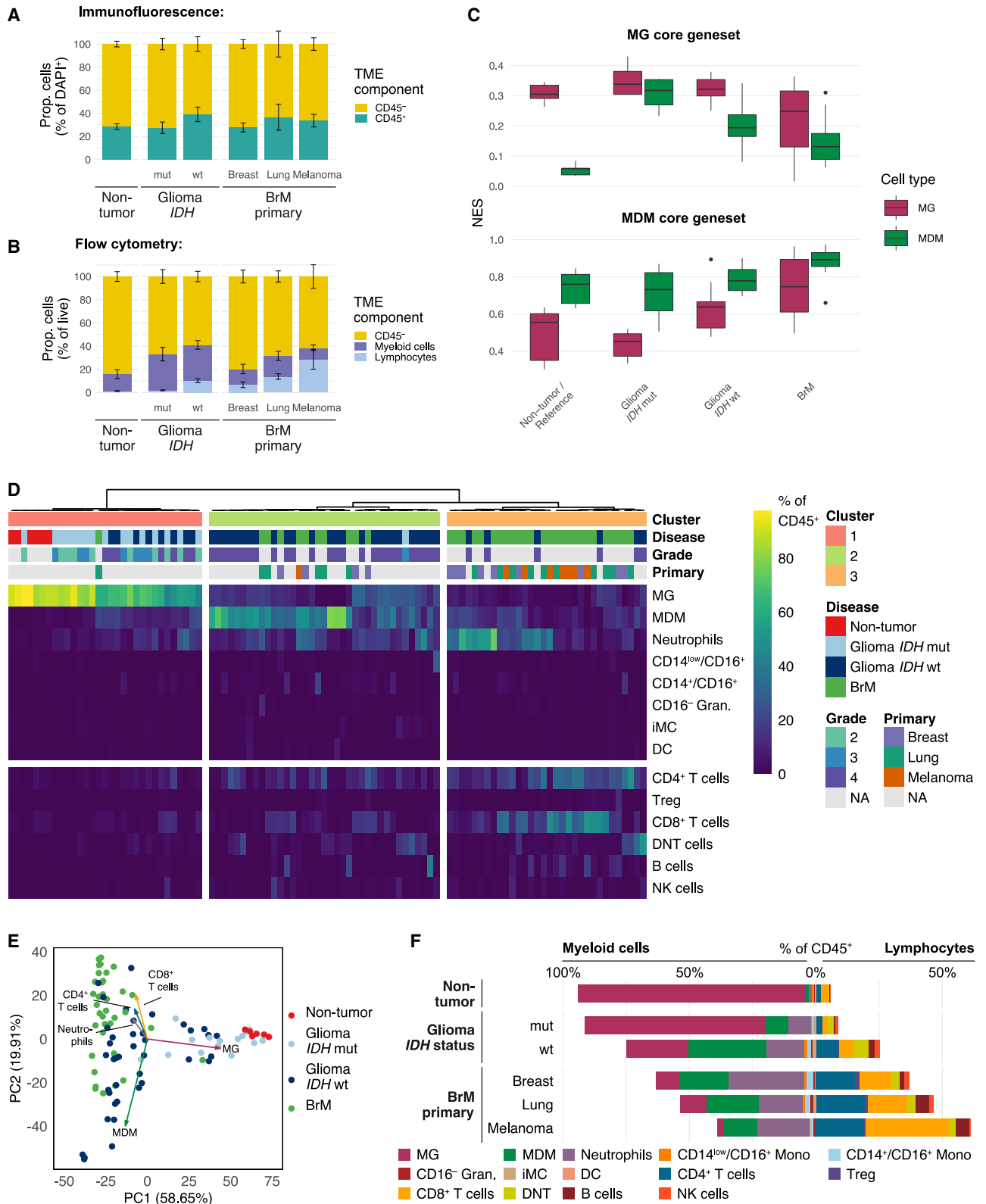
(legend on next page)

Immune checkpoint blockade (ICB), adoptive cell therapy, and vaccines represent treatments targeted against immune cells within the TME and systemically. The success of immunotherapies in certain extracranial cancers has led to clear motivation for their evaluation in brain malignancies. However, although they show some clinical efficacy in a subset of BrM patients (Hendriks et al., 2019; Long et al., 2018; Tawbi et al., 2018), ICB has only resulted in responses in isolated cases of primary gliomas to date (Lim et al., 2018; Schalper et al., 2019). Beyond tumor cell-intrinsic effects, this may be attributed in part to immune-suppressive components of the brain TME, including tumor-associated macrophages (TAMs), which have emerged as prominent players in brain cancers (Gutmann and Kettenmann, 2019; Quail and Joyce, 2017).

Lineage-tracing experiments in mice revealed that brain TAMs can originate from tissue-resident MG or monocyte-derived macrophages (MDMs) recruited from the peripheral circulation (Bowman et al., 2016; Chen et al., 2017). TAMs are highly plastic cells that integrate input from cytokines, growth factors, and other stimuli, resulting in diverse activation states and cellular phenotypes, including promotion of invasion, angiogenesis, metastasis, and immune suppression (Mantovani et al., 2017; Noy and Pollard, 2014). This plasticity and their position at the nexus between malignant cells and tumor-infiltrating T cells makes TAMs a promising target of TME-directed therapies in different cancers. Indeed, studies in mice showed that phenotypic alteration of TAMs results in anti-tumor efficacy in glioblastoma (Pyonteck et al., 2013; Quail et al., 2016; Yan et al., 2017), whereas TAM depletion prevents BrM outgrowth (Qiao et al., 2019).

Despite these preclinical studies, the precise contribution of the two ontogenetically distinct TAM cell types in human brain malignancies is unclear, which hinders clinical translation. For example, previous studies interrogating the role of TAMs in patient brain tumors did not distinguish between MG and MDMs based on use of lineage tracing-derived markers (Gabrusiewicz et al., 2016; Sankowski et al., 2019; Szulzewsky et al., 2016) or focused solely on gliomas (Müller et al., 2017; Venteicher et al., 2017). We therefore interrogated the TME landscape in gliomas and BrMs, with an emphasis on exploring TAMs, while also investigating their relation to other immune cells and structures in the TME. We leveraged this multimodal resource to address a number of questions. Do tumors arising within the brain shape their TME differently than cancers that metastasize from extracranial sites? Does *IDH* mutation status affect the TME? How do distinct TME compositions potentially modulate the activation states of immune cells? By integrating the answers to these questions, we provide insights into potential strategies to harness the brain TME in the fight against these deadly diseases.

RESULTS

Tumor Origin and *IDH* Mutational Status Influence the Immune Composition of Brain Malignancies

We first determined the broad immune cell abundance in the brain TME by analyzing the pan-leukocyte marker CD45 through immunofluorescence (IF) staining of whole-tissue sections and flow cytometry (FCM) analyses of non-tumor brain tissue, *IDH* mut low-grade and *IDH* WT high-grade gliomas, and BrMs originating from different primaries, including breast cancer, lung cancer, and melanoma (Figures 1A, 1B, and S1A). This showed a leukocyte abundance from ~20%–40% across the cancer samples. Stratification of CD45$^+$ cells into myeloid and lymphoid lineages revealed a significant increase in myeloid cells in *IDH* mut and *IDH* WT gliomas and of lymphocytes in *IDH* WT tumors and BrMs compared with non-tumor tissue (Figure 1B; p < 0.05, one-sided Student's t test). We used multicolor fluorescence-activated cell sorting (FACS) to analyze 14 major immune cell populations across 100 clinical samples (Figure S1A; Tables S1 and S2) and collected cells for RNA sequencing (RNA-seq) from 48 patients (Table S3; full clinical annotation).

By incorporating cell lineage tracing and mouse models of high-grade gliomas and BrM, we previously identified the cell surface marker integrin alpha 4, *ITGA4/CD49D*, as a means to discriminate tumor-associated MG (T-MG) from tumor-associated MDMs (T-MDMs) (Bowman et al., 2016), which we integrated here into clinical sample analyses. This enabled sorting of CD45$^-$ non-immune cells, CD49D^{low} MG, CD49D^{high} MDMs, neutrophils, and CD4$^+$ and CD8$^+$ T cells (Figure S1A; Tables S2 and S3A) for transcriptome analysis by RNA-seq. We assessed sorting fidelity by FCM re-analysis of the sorted CD49D^{low} and CD49D^{high} TAM populations (purity, 98.4%–99.8%) and by investigating the frequency of the canonical *IDH* codon 132 missense mutation in the RNA-seq reads from CD45$^-$ cells and CD49D^{low} and CD49D^{high} TAM populations. Although we

Figure 1. The Immune Cell Composition of Brain Malignancies

(A) Quantification of immunofluorescence (IF) staining of non-immune (CD45$^-$) and immune cells (CD45$^+$) in sections of non-tumor brain tissue (n = 6), gliomas (n$_{IDH\ mut}$ = 16, n$_{IDH\ WT}$ = 16), and brain metastases (BrMs, n$_{breast}$ = 12, n$_{lung}$ = 5, n$_{melanoma}$ = 7). Data are represented as mean ± SEM.

(B) Flow cytometry (FCM) quantification of non-immune cells (CD45$^-$), myeloid cells (CD45$^+$, CD11B$^+$), and lymphocytes (CD45$^+$, CD11B$^-$) in non-tumor tissue (n = 6), gliomas (n$_{IDH\ mut}$ = 17, n$_{IDH\ WT}$ = 40), and BrMs (n$_{breast}$ = 13, n$_{lung}$ = 16, n$_{melanoma}$ = 8). Data are represented as mean ± SEM.

(C) Gene set variation analysis (GSVA) normalized enrichment score (NES) of MG and MDM ontogeny-specific core gene signatures in CD49D^{low} MG and CD49D^{high} MDMs from non-tumor and tumor tissues.

(D) Heatmap of immune cell proportions in relation to all CD45$^+$ cells (MG, microglia; MDM, monocyte-derived macrophage; CD14^{low}/CD16$^+$, CD14^{low}/CD16$^+$ monocyte; CD14$^+$/CD16$^+$, CD14$^+$/CD16$^+$ monocyte; CD16$^-$ Gran., CD16$^-$ granulocyte; iMC, immature myeloid cell; DC, dendritic cell; Treg, regulatory T cell; DNT, double-negative T cell) across the cohort (n$_{non-tumor}$ = 6, n$_{glioma}$ = 57, n$_{BrM}$ = 37). Cluster assignment, disease type, *IDH* mutation status, and BrM primary tumor are annotated per column (for clinical information, see Table S1).

(E) Principal component (PC) biplot of FCM data with sample scores and top 5 loadings of the first two PCs (n = 100 clinical samples, proportion of variance shown on PC axes).

(F) Mean of immune cell populations in non-tumor tissue (n = 6), gliomas (n$_{IDH\ mut}$ = 17, n$_{IDH\ WT}$ = 40), and BrMs (n$_{breast}$ = 13, n$_{lung}$ = 16, n$_{melanoma}$ = 8) as percentage of CD45$^+$ cells.

See also Figure S1 and Tables S1 and S2.

observed a mean mutated allele frequency of 0.43 in CD45$^-$ cells from IDH mut gliomas (range, 0.3–0.61), this was very rare in TAMs (mean, 0.01; range, 0.0–0.09), indicating reliable separation of cell populations. In a t-distributed stochastic neighbor embedding (t-SNE) visualization of sorted populations, samples clustered mostly by cell type (Figure S1B), with gliomas and BrMs discernible as separate groups in the CD45$^-$ population.

In this global expression analysis in the context of the other major brain TME components, CD49D^{low} and CD49D^{high} TAM populations clustered closely, suggesting broad transcriptomic similarity. We thus further interrogated the utility of CD49D to differentiate between TAM populations by analyzing association of MG- and MDM-specific ontogeny core gene sets, identified previously from lineage-tracing studies (Bowman et al., 2016), in human CD49D^{low} and CD49D^{high} cells sorted from non-malignant and brain cancer tissues. This revealed enrichment of ontogeny core gene sets in the corresponding cell type (Figure 1C), demonstrating our ability to accurately distinguish MG and MDMs in human samples across different disease entities. Interestingly, these core signatures were influenced within certain tumor types, with T-MDMs showing an increased MG core gene set signal in IDH mut gliomas and T-MG acquiring MDM features in BrMs, suggesting tissue-dependent transcriptional programming of these cells, as further interrogated below.

We next assessed the landscape of intratumoral immune cell populations (Figure S1A; Table S2) using clustering analysis to identify patterns of cellular abundance (Figure 1D; chi-square test for independence, p < 0.0001). This revealed three major clusters: (1) non-tumor samples and IDH mut gliomas characterized by dominance of MG with low numbers of other immune cells; (2) IDH WT gliomas and several BrMs with an influx of MDMs and, to some extent, neutrophils into the tumor while mostly excluding lymphocytes; and (3) predominantly BrMs and few IDH WT gliomas exhibiting the most diverse immune cell landscape with substantial infiltration of T cells and neutrophils. Certain tumors contained CD14^{low}/CD16$^+$ non-classical monocytes, CD14$^+$/CD16$^+$ intermediate monocytes, CD16$^-$ granulocytes, dendritic cells (DCs), or immature myeloid cells. Across all samples, the lymphocyte compartment was mostly composed of T cells with fewer natural killer (NK) cells and B cells.

Principal-component analysis (PCA) of the relative abundance of all investigated populations confirmed that MG, MDMs, neutrophils, and CD4$^+$ and CD8$^+$ T cells are the major immune cell determinants of the brain TME landscape (Figure 1E). Principal component 1 (PC1) separated non-tumor tissue and IDH mut gliomas from IDH WT gliomas and BrMs, whereas PC2 distinguished IDH WT gliomas and BrMs. Further analysis stratifying for IDH status in gliomas and the primary tumor site in BrMs verified a substantially higher proportion of lymphocytes in BrMs (Figure 1F; mean$_{lymphocytes \ \%CD45}^+$ = 46.23%, SEM = 4.15, t test, p < 0.0001). Melanoma BrMs exhibited the most abundant lymphocyte infiltrate with a sizeable CD8$^+$ T cell fraction (mean$_{CD8^+ \ \%CD45}^+$ = 33.01%, SEM = 5.82, one-way ANOVA, p < 0.01). Regulatory T cells (Tregs) were detected in certain BrMs (mean$_{Treg \ \%CD45}^+$ = 1.2%, SEM = 0.36) but were rare in gliomas (mean$_{Treg \ \%CD45}^+$ = 0.25 %, SEM = 0.05, t test, p < 0.05).

Because of the prominence of T-MG and T-MDMs in the myeloid compartment of brain malignancies, we used IF staining

and deconvolution analyses to independently validate their presence. Commonly employed MG markers, such as P2RY12, TMEM119, and SALL1, and MDM-associated genes, such as AHR and VDR, showed varying RNA expression levels across different brain malignancies while maintaining their cell type specificity (Figure S2A) in a similar manner as observed for the ontogeny core gene sets (Figure 1C). An equivalent pattern was observed at the protein level (Figure S2B), where P2RY12 showed the highest expression in non-tumor tissue, and CD68 was most abundant in BrM-TAM populations. This necessitated use of both markers complemented by CD49D to reliably identify MG and MDMs in IF analyses (Figure S2C). We used this strategy to interrogate a cohort of non-tumor, glioma, and BrM samples by whole-section quantification, confirming MDM accumulation in IDH WT gliomas and BrMs (Figures 2A–2C). Furthermore, comparison of tissue processed independently for IF and FCM from the same individual samples demonstrated significant concordance (Figure S2D).

We queried the sorted cell populations for T-MG- and T-MDM-specific differentially expressed genes (DEGs) that separate these two populations from the most abundant other cell types; i.e., CD45$^-$ cells, neutrophils, and T cells (Figure S2E). Several of the genes highly expressed in T-MG are well-established MG markers (P2RY12, TMEM119, and TAL1), whereas genes highly expressed in T-MDMs include markers of alternative macrophage polarization (FCGR2B and CLEC10A) and DC-like phenotypes (CD1C, CD1B, and CD207) with increased phagocytic and antigen cross-presentation ability (CD209). These gene sets also allowed us to utilize a publicly available integrated dataset (Vivian et al., 2017) containing bulk expression data of healthy cortical brain tissue from the Genotype-Tissue Expression project (GTEx; GTEx Consortium, 2013) and low- and high-grade glioma samples from The Cancer Genome Atlas (TCGA; Ceccarelli et al., 2016) in a bulk tissue transcriptome deconvolution approach (Racle et al., 2017). The estimates obtained of MG and MDM proportions in this external dataset (n = 711 samples) verified the prevalence of MG in IDH mut gliomas and MDM enrichment in IDH WT gliomas (Figure 2D).

MG and MDMs Exhibit a Multifaceted Polarization Phenotype in Brain Malignancies

We next employed PCA to specifically focus on TAMs and analyze genes whose expression was influenced by tissue type (i.e., reference MDMs, non-tumor brain, gliomas, and BrMs) and cell type (i.e., MG and MDMs) (Figure 3A). Within the first two PCs, MG and MDMs projected into different spaces, with in vitro differentiated MDMs distinct from tissue-derived samples. We observed a gradient across PC1 with non-tumor brain tissue at one end, traversing IDH mut and IDH WT gliomas, and ending with BrMs. Thus, TAM transcriptomic changes are influenced by the brain TME per se and also by the specific type of malignancy.

We contrasted T-MG and T-MDMs from BrMs or gliomas (regardless of IDH mutation status) with MG from non-tumor brain or in vitro differentiated MDMs from healthy donors, respectively (Figure S3A; Tables S3A and S4). This revealed profound expression changes in both populations, with T-MDMs exhibiting a higher magnitude in their transcriptional response
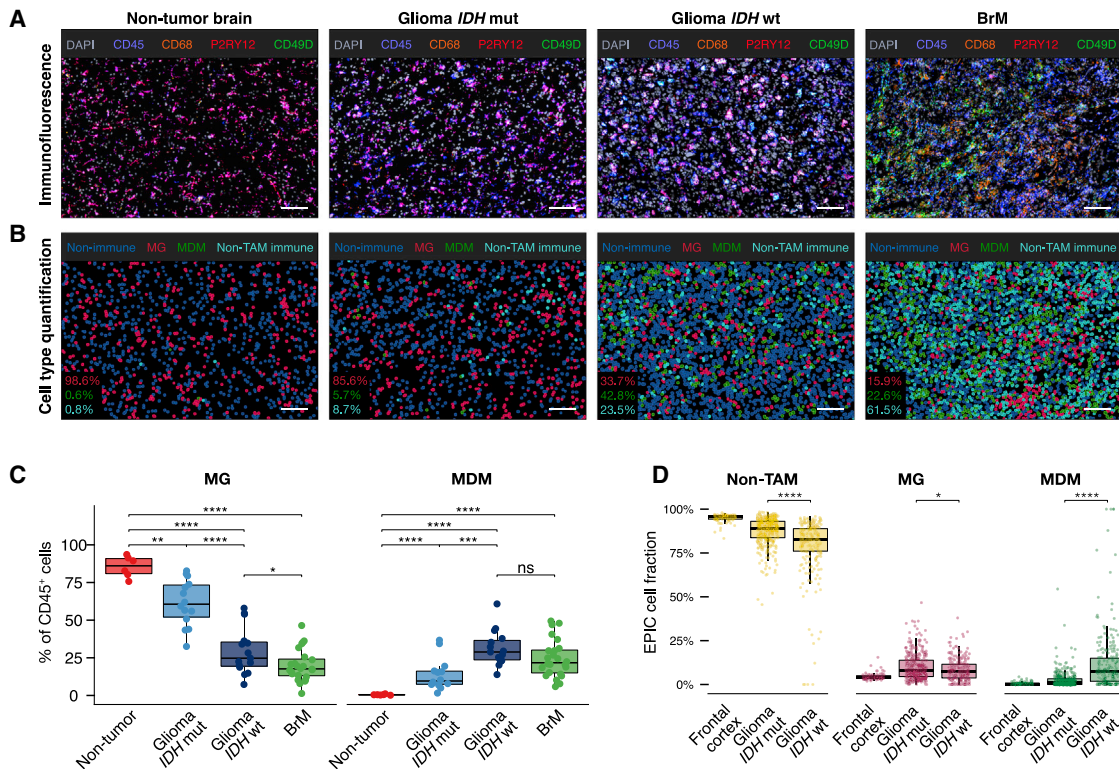
Figure 2. Analysis of MG and MDM Abundance

(A and B) Representative IF images (A) and corresponding cell type identification (B) of MG (CD45$^+$, P2RY12$^+$/CD68$^+$, CD49D$^-$), MDMs (CD45$^+$, P2RY12$^+$/CD68$^+$, CD49D$^+$), and non-immune (CD45$^-$) and non-TAM immune cells (CD45$^+$, P2RY12$^-$/CD68$^-$, CD49D$^{-/+}$) in non-tumor brain tissue, *IDH* mut and *IDH* WT gliomas, and BrMs. Scale bars, 100 μm. Insets show quantification per field of view (FOV).

(C) IF quantification of MG and MDM abundance in non-tumor brain tissue (n = 6), *IDH* mut (n = 16) and *IDH* WT (n = 16) gliomas, and BrMs (n = 24).

(D) Deconvolution of merged GTEx and TCGA glioma datasets, showing relative abundance of MG, MDMs, and non-TAMs ("other cells") in healthy frontal cortex and *IDH* mut and *IDH* WT gliomas.

Wilcoxon rank-sum test was used for statistical analysis: *p < 0.05, **p < 0.01, ***p < 0.001, ****p < 0.0001. See also Figure S2.

compared with T-MG (Figure S3A). The intersect of DEGs in gliomas and BrMs was highest in T-MDMs (Figure S3B), potentially reflecting the greater changes experienced by these cells upon entering the completely foreign environment of a brain tumor. This was also evident when focusing on genes upregulated in gliomas and BrMs that are exclusive to T-MG or T-MDMs (Figure 3B). In T-MG and T-MDMs, the number of shared genes was higher across different diseases than between these two cell populations within the same tumor type. Consequently, only a small number of genes (n = 137) showed concordant upregulation across a comparison of all diseases and TAM types (Figure 3B).

To explore the underlying biological processes conserved in gliomas and BrMs, we examined the intersect of upregulated genes (Figure S3B) in T-MG or T-MDMs using gene set over-representation analysis (ORA). In the Molecular Signature Database (MSigDB; Liberzon et al., 2015) "hallmark" collection of major biological categories, T-MG and T-MDMs showed pathway enrichment in (1) modeling of the TME ("Angiogenesis," "Hypoxia"), (2) inflammation ("Inflammatory Response," "Allograft Rejection"), and (3) immune cell activation states ("TNFα Signaling via NFκB," "Interferon α Response," "Interferon γ

Response," "IL2 STAT5 Signaling," and "IL6 JAK STAT3 Signaling") (Figure S3C).

We also assessed the M1 and M2 polarization status of T-MG and T-MDMs using a panel of marker genes (Murray et al., 2014). However, no evident pattern emerged of a defined M1 versus M2 phenotype in glioma or BrM T-MG or T-MDMs (Figure S3D). To further explore the activation state of T-MG and T-MDMs, we subjected their respective upregulated genes to ORA of macrophage stimulus-specific programs (Xue et al., 2014). This revealed a multifaceted response (Figure 3C) incorporating canonical M1 (interferon γ [IFNγ]) and M2 polarization (interleukin-4 [IL-4]), including expression changes associated with chronic inflammatory stimuli (tumor necrosis factor alpha [TNF-α] + prostaglandin E [PGE$_2$] and TNFα + PGE$_2$ + Pam3CysSerLys4 [TPP]) and exposure to free fatty acids (oleic acid [OA] and palmitic acid [PA]), which have been implicated in modulating myeloid cell function (Thapa and Lee, 2019). This indicates diverse transcriptional programming of T-MG and T-MDMs in gliomas and BrMs extending beyond simple M1 versus M2 polarization.

To understand which processes are linked to and potentially driving these responses, we identified the gene set enrichment
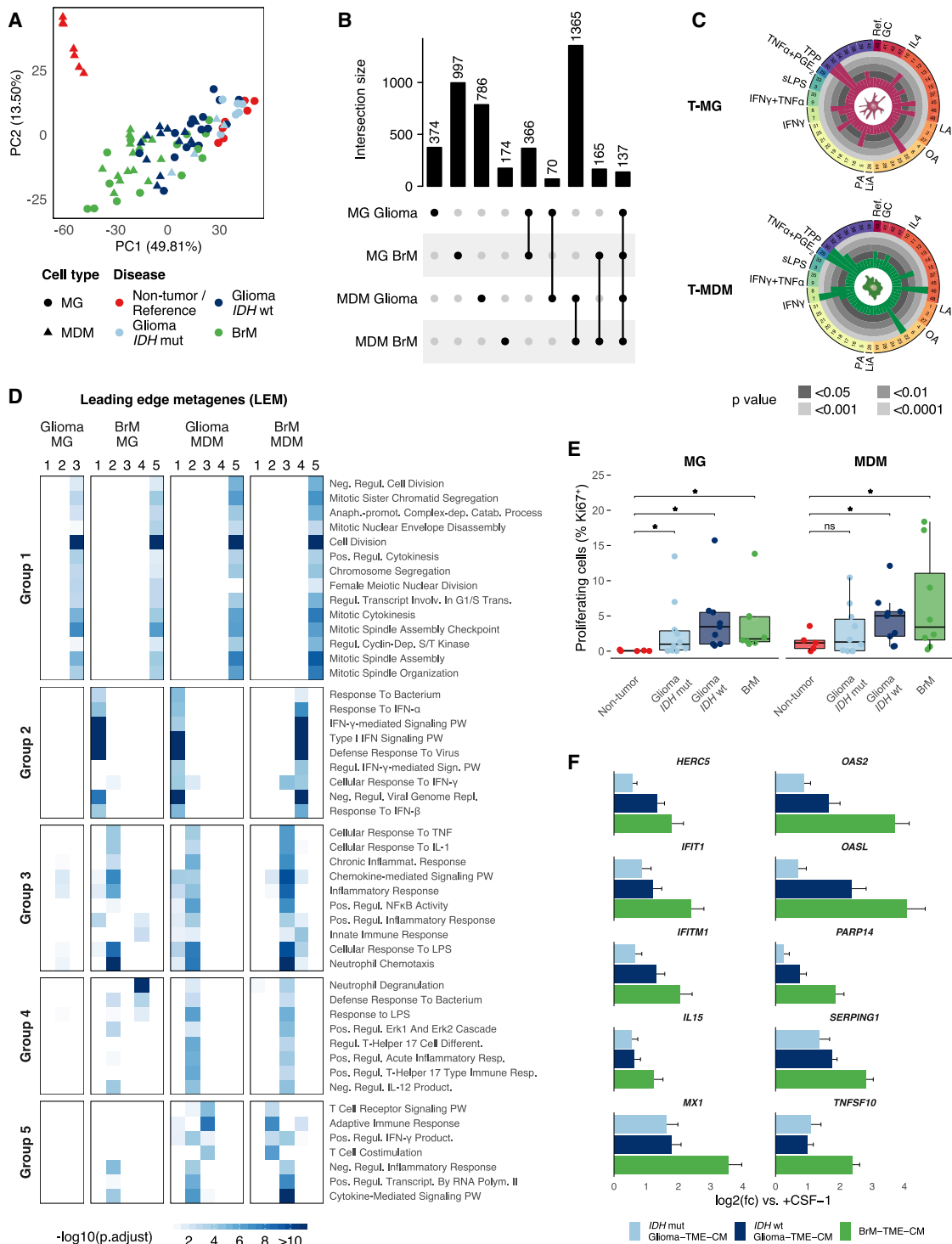
Figure 3. MG and MDMs Exhibit a Multifaceted Polarization Phenotype in Brain Malignancies

(A) PC biplot of MG and MDM transcriptome data from non-tumor brain tissue, *IDH* mut and *IDH* WT gliomas, and BrMs (for clinical information, see Table S3A; reference = *in-vitro*-generated MDMs; proportion of variance shown on PC axes).

(B) Visualization of intersects of the conserved sets of significantly upregulated genes in MG and MDMs. Intersects between sets are shown in the combination matrix. n_{genes} found uniquely in a gene set or intersect is indicated above individual bars.

(C) Stimulus-specific macrophage gene expression modules overrepresented (within conserved differentially expressed genes [DEGs] versus respective references) in tumor associated MG (T-MG) and tumor-associated MDMs (T-MDMs). Bar heights and color indicate significance level. GC, glucocorticoid; IFNγ,

(legend continued on next page)

analysis (GSEA; Subramanian et al., 2005) leading-edge genes in T-MG and T-MDMs in gliomas and BrMs and clustered them into leading-edge metagenes (LEMs) with non-negative matrix factorization (Godec et al., 2016). This identified up to 5 distinct LEMs per cell type and comparison that were tested for significant overlap in a pairwise fashion (Figure S3E) and annotated using Gene Ontology (GO) terms (Figure 3D). LEMs associated with mitosis and cell proliferation were present in T-MG and T-MDMs in gliomas and BrMs (Figure 3D, group 1). The biological validity of these LEMs were verified by staining for Ki-67, a marker of cell proliferation, in non-tumor, glioma, and BrM tissue sections (Figure 3E), showing increased proliferation in T-MG and T-MDMs in *IDH* WT gliomas and BrMs and in T-MG in *IDH* mut gliomas.

Interestingly, LEMs enriched for type I IFN signaling were detected in glioma and BrM T-MDMs and in BrM T-MG but not in glioma T-MG (Figure 3D, group 2). Sustained type I IFN signaling has been implicated in mediating immune suppression and ICB resistance (Benci et al., 2016). The stringency of these group 2 LEMs was validated by building a protein-protein interaction (PPI) network of the shared LEM genes (Figure S3F). Beyond their role in antiviral responses, the genes highlighted at the center of the PPI network (Figure S3F, red nodes) have been implicated in a variety of tumor-promoting and -suppressing roles (Benci et al., 2016). Similarly, the more peripheral network nodes *IL15* and *TNFSF10* are potentially able to modulate an effective immunological anti-tumor response or induce apoptosis in cancer cells, respectively (Bouralexis et al., 2005; Santana Carrero et al., 2019). We asked whether these genes were directly induced by secreted factors in the brain TME and established cell-based assays to expose MDMs to TME conditioned medium (CM) generated from single-cell suspensions of freshly isolated glioma or BrM samples in culture. All genes analyzed were upregulated by BrM-TME-CM and to a lesser extent by glioma TME-CM (Figure 3F). We also detected induction of inflammation- and nuclear factor κB (NFκB) signaling-associated LEMs in BrM-MG, glioma MDMs, and BrM-MDMs (Figure 3D, group 3). LEMs that point toward a Th17 response (group 4) and recruitment of immune cells and interactions between different immune cell compartments were exclusively detected in MDMs (group 5). Collectively, these analyses reveal acquisition of a multifaceted activation state of MG and MDMs upon their integration into the TME of brain malignancies.

IDH Mutation Status Associated with Changes in Glioma TAM Activation
We next asked whether MG and MDMs occupy distinct regions within the TME of *IDH* WT gliomas. Spatial analysis of tissue sections showed significant enrichment of both populations in the perivascular niche (Figures 4A and S4A). Analysis of their distribution relative to CD31⁺ vascular structures showed a closer proximity of T-MDMs compared with T-MG (Figures 4B and S4A). Interrogation of anatomical transcriptome data from the Ivy Glioblastoma Atlas Project (Ivy GAP) study (Puchalski et al., 2018) also demonstrated enrichment of T-MDMs in the microvascular compartment (Figure S4B). This enrichment coincided with CD4⁺ and CD8⁺ T cells, indicating further spatial TME organization in *IDH* WT gliomas.

We assessed whether the distinct T-MG and T-MDM distributions and cell numbers are paralleled by their activation state. In the LEM analysis, we had detected a type I IFN response in glioma MDMs but not MG (Figure 3D); we therefore queried the FCM data to analyze levels of major histocompatibility complex (MHC) class II human leukocyte antigen-DR isotype (HLA-DR) expression. This showed significantly increased HLA-DR in T-MDMs compared with T-MG in *IDH* mut and *IDH* WT tumors (Figure 4C). We screened the associated RNA-seq data for antigen processing and presentation pathway gene sets using GSEA and gene set variation analysis (GSVA) (Figure 4D). Interestingly, we found evidence of increased expression of MHC class II antigen presentation gene sets in *IDH* WT glioma MDMs and also antigen processing-associated pathways (Figure S4C) and MHC class I presentation gene sets (Figure 4D). Although these findings suggest the potential of TAMs, particularly T-MDMs, to initiate an immune response, this potential is generally not realized in the glioma TME, based on the current status of ICB trials in this disease, and we thus asked whether there was also evidence of pro-tumor states in these cell populations.

We compared T-MG and T-MDMs from *IDH* WT gliomas with T-MG from *IDH* mut gliomas because they constitute the most abundant TME cell types in these tumors, respectively (Figures 1F and 2C; Table S5). This revealed 489 DEGs in T-MG (Figure 4E; Table S5; 406 up- and 83 downregulated), and 1,478 DEGs in T-MDMs (Figure 4F; Table S5; 903 up- and 575 downregulated). Although these gene lists were generated by comparing T-MDMs from *IDH* WT gliomas with T-MG from *IDH* mut gliomas, they similarly separated T-MDMs in *IDH* mut versus *IDH* WT disease in a clustering analysis (Figure 4F), indicating that they indeed reflect T-MDM alterations based on the *IDH* status of the tumor. 421 genes exhibit a similar pattern across both TAM cell types (343 up- and 78 downregulated), suggesting that T-MG and T-MDMs can also acquire a common transcriptional pattern in *IDH* WT tumors. Among the shared genes were several encoding extracellular matrix (ECM) proteins (Figure 4G, *FN1* and *VCAN*) and ECM-associated matricellular proteins (*THBS1*, *TGFBI*, *LGALS3*, and *ANGPTL4*) that regulate the availability of ECM-sequestered ligands, angiogenesis, and tumor

---

interferon gamma; LA, lauric acid; LiA, linoleic acid; OA, oleic acid; PA, palmitic acid; PGE₂, prostaglandin E₂; sLPS, standard lipopolysaccharide; TNF-α = tumor necrosis factor alpha; TPP, TNFα + PGE₂ + Pam3CysSerLys4; IL-10, interleukin 10.

(D) Heatmap of GO overrepresentation analysis of leading-edge metagenes (LEMs) in MG and MDMs from gliomas and BrMs. Tile fill indicates significance (hypergeometric test, -log10 (adjusted p value), terms were filtered by significance).

(E) IF quantification of the proportion of proliferating Ki67⁺ MG and MDMs in non-tumor tissue (n = 5), *IDH* mut (n = 10) and *IDH* WT gliomas (n = 9), and BrMs (n = 8). Means were compared with one-tailed t test: *p < 0.05.

(F) qRT-PCR of type I IFN LEM marker genes from group 2 (Figure S3F) in *in-vitro*-generated MDMs stimulated with the indicated TME culture-conditioned medium (TME CM). Fold changes were calculated relative to colony-stimulating factor-1 (CSF-1)-treated MDM baseline (one-way ANOVA, p < 0.1, n_MDM = 4–11). Data are represented as mean ± SEM.

See also Figure S3 and Table S4.
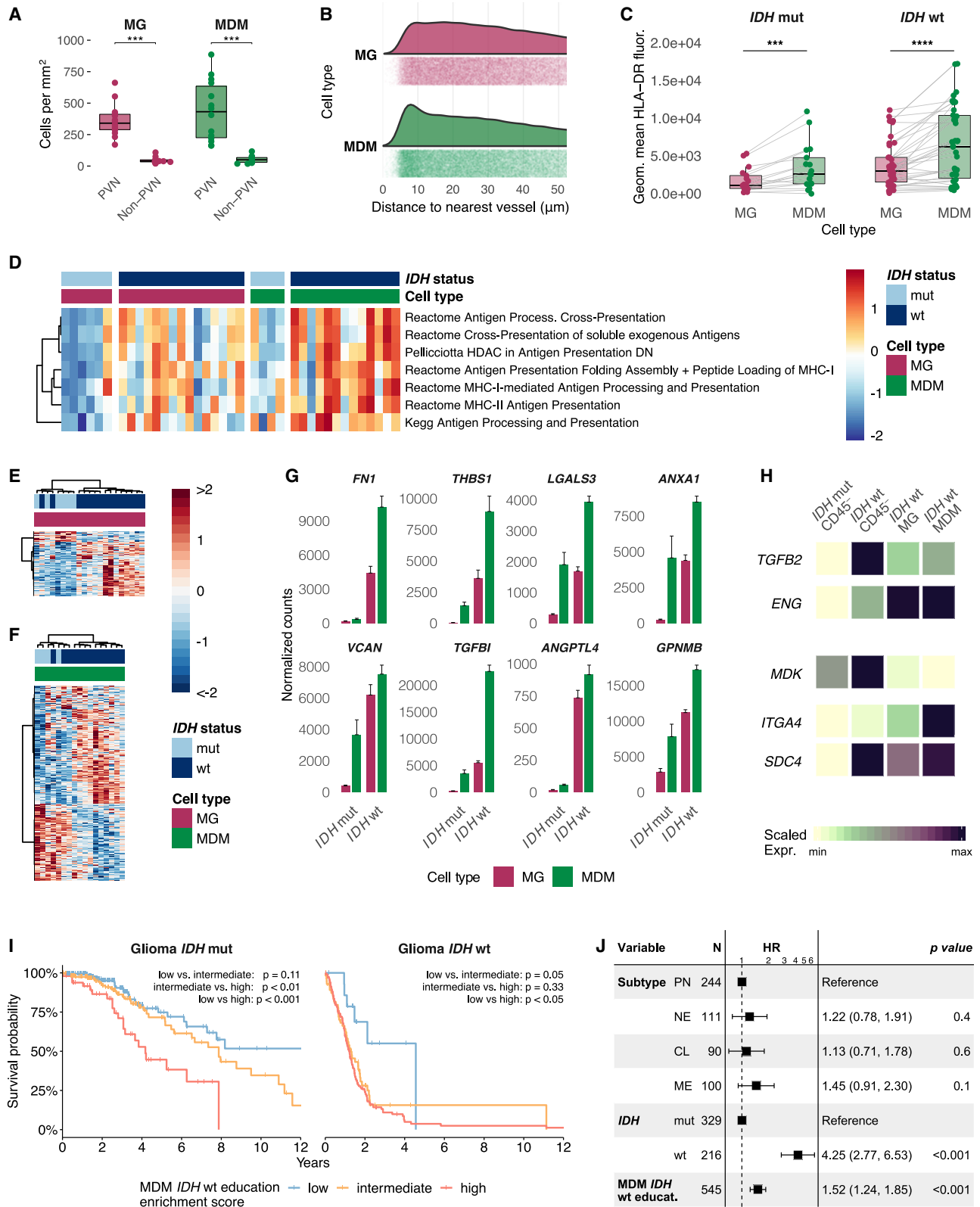
(legend on next page)

immunity (Mushtaq et al., 2018). This suggests that TAMs help shape the composition and effector functions of ECM proteins in *IDH* WT tumors. We also found the anti-inflammatory molecules *ANXA1* and *GPNMB* (Figure 4G), previously implicated in pro-tumorigenic macrophage polarization and inhibition of T cell activation (Kobayashi et al., 2019; Ripoll et al., 2007), to be upregulated in T-MG and T-MDMs.

We next investigated inflammation mediators within the CD45− population of *IDH* WT tumors in parallel with their corresponding receptors in TAMs. *TGFB2* expression was elevated compared with *IDH* mut CD45− cells, and the accessory transforming growth factor β (TGF-β) receptor *ENG* was highly expressed in *IDH* WT TAMs (Figure 4H). TGFB2 has pleiotropic effects in inflammation and tissue remodeling during wound healing and has been implicated in an autocrine signaling loop in glioblastoma cells (Rodón et al., 2014). The neuroinflammatory cytokine *MDK*, which modulates TAM polarization to a M2-like phenotype in glioma (Meng et al., 2019), was upregulated in CD45− cells from *IDH* WT tumors, and its receptors *SDC4* and *ITGA4/CD49D* were differentially expressed in T-MDMs versus T-MG (Figure 4H), suggesting cell-type-specific effects of this inferred signaling loop.

We asked whether a T-MDM-specific gene set generated from *IDH* WT gliomas was associated with a survival difference in patients. By logistic regression, we derived a representative signature consisting of 36 genes (Figure S4D) from the total number of genes upregulated in TAMs in brain malignancies (Figure 3B). This included the macrophage marker *RUNX3*; the atypical chemokine receptor *ACKR3*, which can regulate CXCL12-CXCR4 signaling; the endoplasmic reticulum (ER) stress protein *HERPUD1* and the inhibitory Fc receptor *FCGR2B*, which can modulate macrophage activation (Bournazos et al., 2016; Li et al., 2018); and the cytokine *IL19*, which affects angiogenesis and macrophage polarization (Richards et al., 2015). The signature was used to classify patients in a merged TCGA dataset of low- and high-grade gliomas (Figures 4I and S4E). In *IDH* mut patients, a decrease in median overall survival was associated with enrichment of the T-MDM *IDH* WT signature, whereas *IDH* WT patients with a low enrichment score showed increased survival. This

was confirmed in a multivariate Cox proportional hazard model that included the transcriptomic glioma subtypes (as annotated in the TCGA dataset) and *IDH* status (Figure 4J). To verify that this effect did not simply reflect changes in T-MDM number, we classified the TCGA cohort based on enrichment of the T-MDM-specific gene set used for deconvolution, which showed a low effect on survival (Figure S4F).

In light of disappointing outcomes from PD1 or PDL1 ICB trials in glioblastoma to date, we queried whether the abundant T-MG and T-MDMs could contribute to the limited therapeutic efficacy. We performed ORA of a panel of 20 gene sets previously associated with innate anti-PD1 resistance (IPRES; Hugo et al., 2016) in the TAM DEGs of *IDH* WT gliomas and found a sizeable fraction to be upregulated in T-MG and T-MDMs (Figure S4G). We then included the CD45− population and interrogated enrichment of IPRES gene sets on the single-sample level by GSVA (Figure S4H). This yielded a diverse picture with tumor cells and TAMs enriched for IPRES gene sets to varying degrees. Therefore, TAMs and CD45− cells from *IDH* WT gliomas may contribute to mediating innate ICB resistance.

The Immune Contexture Influences the TME on a Global Level

Through integrated analysis of protein and gene expression data, we next explored the effect of immune cell infiltration. Of 200 inflammation-associated proteins assessed, 55 were differentially detected in our sample cohort (for clinical information, see Table S3B). Unsupervised clustering analysis revealed distinct clusters with abundant inflammatory proteins in tumors (Figure 5A). The profile of *IDH* WT gliomas and BrMs showed a sizeable overlap (protein cluster 1), encompassing angiogenic factors (VEGFA and ANG), growth factors (PDGFA, TGFB1, SPP1, and GDF15), several proteases and protease inhibitors (SERPINE1, CTSS, and TIMP1), the proteolysis cascade regulator PLAUR, and the cytokines CCL2 and CCL5 (Figures 5A and S5A). However, we also found distinct protein patterns between gliomas and BrMs. The neurotrophic growth factor FGF2 and neuronal cell adhesion molecules, including ALCAM, which regulates immune cell infiltration during

---

Figure 4. *IDH* Mutation Status Shapes TAM Activation in Gliomas

(A) Number of MG and MDMs per square millimeter in the perivascular niche (PVN) or distant from the PVN (non-PVN) in *IDH* WT gliomas by IF staining. Means were compared with Wilcoxon signed-rank test: ***p < 0.001.

(B) Distance of MG and MDMs to the nearest vessel in *IDH* WT gliomas ($n_{samples}$ = 14, n_{MG} = 88,781, and n_{MDM} = 92,969 cells counted).

(C) Boxplot of HLA-DR geometric mean fluorescence intensity measured by FCM in MG and MDMs in *IDH* mut and *IDH* WT gliomas. MG and MDMs from the same samples are connected by lines ($n_{IDH mut}$ = 17, $n_{IDH WT}$ = 39; Wilcoxon signed-rank test: ***p < 0.001, ****p < 0.0001).

(D) GSVA of antigen processing and presentation pathways from the Molecular Signatures Database (MSigDB) "Canonical Pathways" collection with significant differential enrichment between MG and MDMs in *IDH* WT tumors and in MG and MDMs across *IDH* mut and *IDH* WT samples. Columns are ordered by *IDH* mutation status and cell type, and rows (Z score) are hierarchically clustered.

(E and F) Expression heatmap of T-MG (E) and T-MDM (F) DEGs (compared with T-MG in *IDH* mut gliomas) in *IDH* mut and *IDH* WT glioma samples. Columns and rows (Z score) are hierarchically clustered.

(G) Normalized counts of selected genes in MG and MDMs in gliomas stratified by *IDH* status. Data are represented as mean ± SEM.

(H) Relative expression in CD45− MG and MDM cells of ligands and receptors upregulated in CD45− cells in *IDH* WT versus *IDH* mut samples and their matching counterparts. Variance-stabilized expression values were scaled to the expression range.

(I) Kaplan-Meier estimator of survival in the TCGA glioma cohort based on enrichment for the MDM *IDH* WT signature, assessed by GSVA in *IDH* mut and *IDH* WT gliomas from the combined TCGA cohort. GSVA scores were separated into tertiles across the combined *IDH* mut and *IDH* WT sample set. Pairwise p values were calculated using a log rank test.

(J) Hazard ratios of a multivariate Cox proportional hazards model with transcriptomic subtype (TCGA annotation), *IDH* status (TCGA annotation), and T-MDM *IDH* WT GSVA score as covariates for overall survival within the TCGA glioma cohort (PN, proneural; NE, neural; CL, classical; ME, mesenchymal subtype).

See also Figure S4 and Table S5.
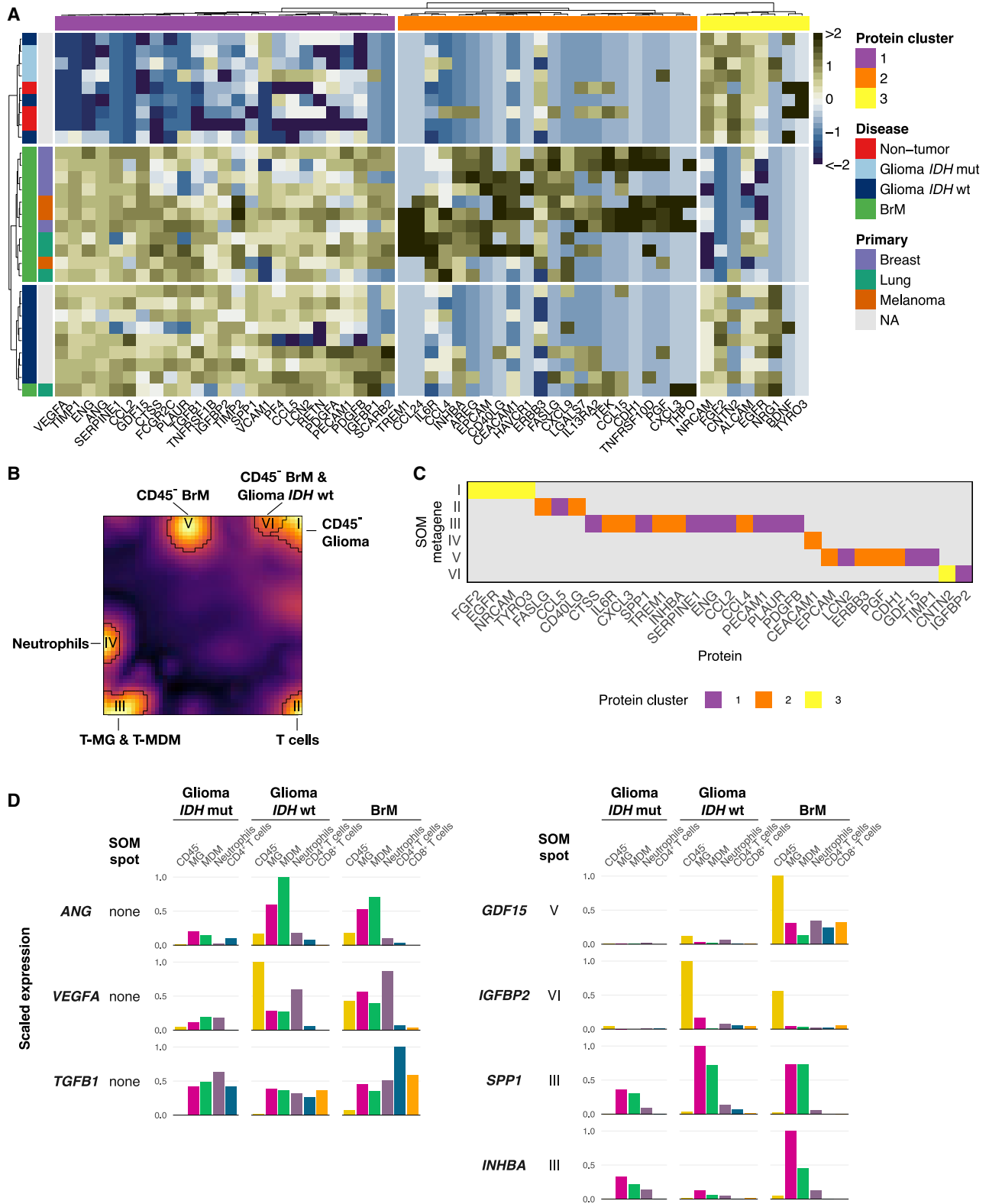
Figure 5. The Immune Contexture Influences the TME on a Global Level

(A) Inflammation-associated bulk tissue protein concentration heatmap subset on 55 proteins with significantly different concentrations between non-tumor brain, gliomas, and BrMs in an ANOVA (p < 0.1, $n_{non-tumor}$ = 3, n_{glioma} = 14, n_{BrM} = 12; concentrations were log10-transformed and Z scored). Rows and columns

(legend continued on next page)

neuroinflammation (Lécuyer et al., 2017), were highly expressed in non-tumor brain, *IDH* mut, and *IDH* WT samples (protein cluster 3; Figure S5A). Conversely, BrM samples had abundant immune-regulatory molecules affecting myeloid and lymphocytic cells and their heterotypic signaling (protein cluster 2; Figure S5A), such as CD40L, IL6R, INHBA, and AREG (Morianos et al., 2019; Zaiss et al., 2015), possibly reflecting the greater immune cell diversity in BrMs. This orthogonal dataset reinforces the RNA-seq analyses showing that inflammatory signaling pathways are highly enriched in brain tumors.

We integrated the cell-type-specific RNA-seq data and bulk protein data to distinguish proteins with more restricted expression versus those that are expressed across a range of cell types. Transcriptome data from CD45$^-$ cells, TAMs, neutrophils, and CD4$^+$ and CD8$^+$ T cells from all tumor samples were clustered using a self-organizing map (SOM). This yielded 6 SOM spots (i.e., metagenes of co-expressed genes; Figure 5B) that recapitulated the respective cell lineages (Figure S5B). The CD45$^-$ populations were assigned to three distinct spots that were associated with more aggressive *IDH* WT gliomas and BrMs (spot VI) or reflected the brain-intrinsic or -extrinsic tumor origin (spots I and V). These cell-type-associated SOM spots overlapped considerably with the protein data (30 of 55 proteins, Fisher's exact test, p < 0.0001; Figure 5C). Although *VEGFA*, *ANG*, and *TGFB1* were expressed by diverse cell types in gliomas and BrMs, other genes, such as *GDF15* and *IGFBP2*, showed more CD45$^-$ cell-restricted expression (Figure 5D). The significant contribution of TAMs to production of key inflammatory proteins, including *SPP1* and *IHNBA*, is reflected by TAM SOM spot III, constituting the largest group of proteins with cell type-specific expression (Figures 5C and 5D).

Myeloid Cells Show a Distinct Phenotype in BrMs

Our global analysis juxtaposing the expression patterns of TAMs in gliomas (regardless of *IDH* status) with BrMs showed disease- and cell-type-specific transcriptomic changes. We thus explored BrM-specific alterations by focusing on genes upregulated only in relation to the corresponding reference and to *IDH* WT gliomas (Figures S6A and S6B; Table S6). Various cytokines, chemokines, and pro-inflammatory molecules were elevated in BrM-MG and BrM-MDMs (Figure 6A), including the potent mediators of autoimmune neuroinflammation *CSF2* and *IL23A* (Zhao et al., 2017) and the pattern recognition receptor *MARCO*. Intriguingly, antibody-mediated MARCO targeting in extracranial tumors increases M1-like polarization of TAMs and enhances ICB efficacy (Georgoudaki et al., 2016). These effects relied on interaction of the antibody with *FCGR2B*, which is also part of the T-MDM *IDH* WT signature (Figures S2E and S4C). Finally, *RETN*, which is involved in

systemic inflammatory disorders (Filková et al., 2009), was up-regulated in BrM-TAMs (Figure 6A).

Analysis of individual BrM-TAM populations uncovered distinct expression patterns. BrM-MG showed restricted upregulation of *IL6* (Figure 6A), which exerts immunosuppressive effects on T cell function in cancer and mediates ICB resistance (Tsukamoto et al., 2018), and the receptor *TREM1*, which modulates pro-inflammatory responses in MG and systemically in myeloid cells during neuroinflammation (Liu et al., 2019; Xu et al., 2019). Among the upregulated chemokines, we found increases in both TAM cell types (*CCL23*) and BrM-MG-restricted (*CXCL5* and *CXCL8*) or BrM-MDM-restricted increases (*CCL8*, *CCL13*, *CCL17*, and *CCL18*) (Figure 6A). These results reveal distinct contributions of TAM populations to the inflammatory TME milieu in a disease-specific manner.

GSEA identified additional cell-type-specific enrichment patterns. BrM-MG showed evidence of IL-6 pathway activity (Figure S6C), and in BrM-MDMs, the "Naba core matrisome" gene set was significantly enriched (Figure S6D). This prompted us to assess expression of genes encoding ECM and matricellular proteins in BrM-MDMs versus BrM-MG, which revealed genes encoding matrix proteins, including type III and IV collagens, *FN1*, the proteoglycans *LUM* and *OGN*, and the matricellular proteins *ECM1*, *SPARC*, and *SPARCL1* as highly expressed in BrM-MDMs (Figure 6B). Although ECM remodeling has been implicated in tumor progression, *LUM*, *OGN*, *SPARCL*, and *SPARCL1* exhibit pro- and anti-metastatic properties, which underscores the complex context-dependent role of the ECM (Kai et al., 2019). We also found high expression of the cathepsin proteases *CTSB* and *CTSW* in BrM-MDMs (Figure 6B), which participate in multiple tumor-promoting processes, including invasion and metastasis (Olson and Joyce, 2015). The hyaluronan receptor *HMMR*, involved in macrophage chemotaxis and fibrosis in lung injury (Cui et al., 2019), was also higher in BrM-MDMs (Figure 6B). Together, these data suggest that the ECM is not only shaped by macrophages at the primary site (Afik et al., 2016) but that T-MDMs may also play a pivotal role in ECM niche construction in BrM that is distinct from *IDH* WT gliomas (Figure 4G).

Given the upregulation of *CXCL8*, a key neutrophil chemoattractant, by BrM-MG (Figure 6A), we explored the TME contribution to recruitment of neutrophils, which were highly abundant in BrM (Figure 1F). Analysis of major neutrophil-recruiting chemokines and their receptors showed broad expression across all interrogated myeloid cells (Figure S6E). To explore the phenotype of BrM-associated neutrophils, we queried the RNA-seq data, which revealed BrM-specific upregulation of *ITGA3* (Figure 6C), which is involved in neutrophil tissue infiltration in sepsis, and *CXCL17*, previously implicated in neutrophil and macrophage recruitment in cancer (Li et al., 2014). We also observed upregulation of the

---

are hierarchically clustered. Clinical data are annotated per row; column annotation reflects the major protein clusters (further information can be found in Table S3B).

(B) Self-organizing map (SOM) of RNA expression data of major cell populations in glioma and BrM samples. SOM spots are highlighted, numbered with Roman numerals, and annotated with their cell type association.

(C) Overlap of individual proteins and SOM spot metagenes; tile color fill reflects protein cluster membership from (A).

(D) RNA-seq counts (normalized, scaled to expression range) of proteins from (A) across major cell types in *IDH* mut and *IDH* WT gliomas and BrMs. SOM spot membership of individual genes is indicated per row.

See also Figure S5.
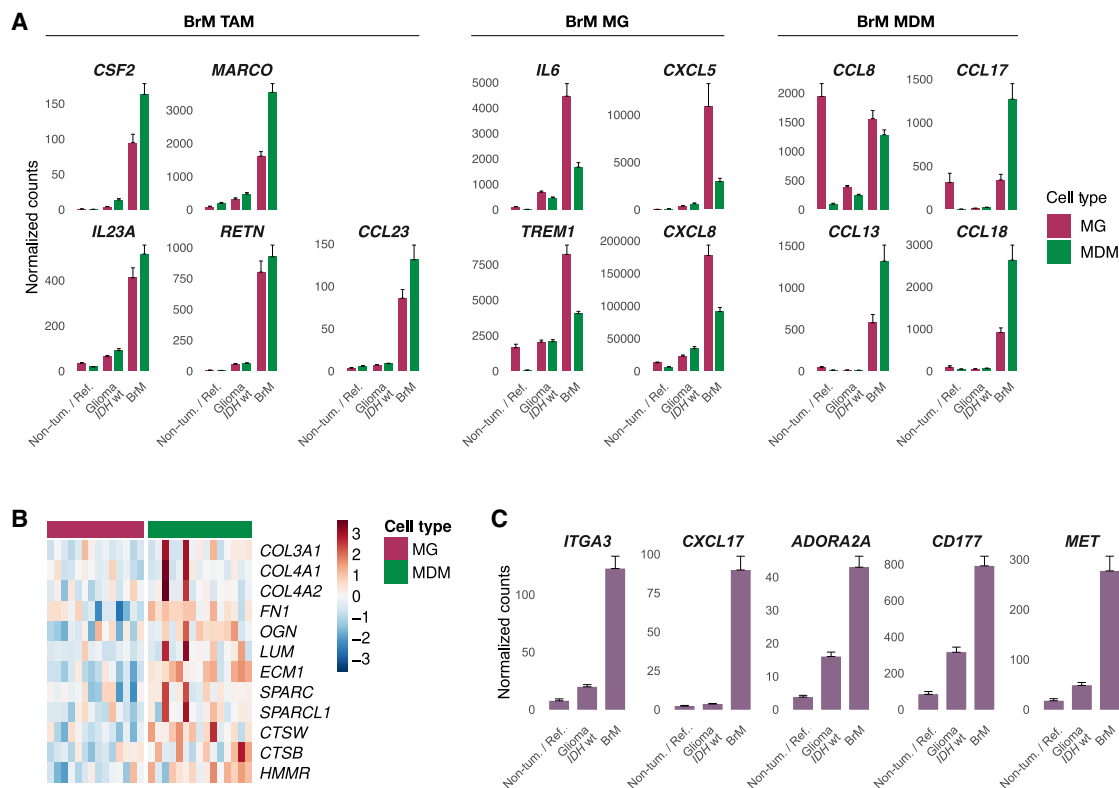
Figure 6. Myeloid Cells Show Distinct Transcriptional Changes in BrMs

(A) Normalized counts of the indicated genes in MG and MDMs in non-tumor or reference, *IDH* WT gliomas, and BrMs. Data are represented as mean ± SEM.

(B) Expression heatmap of Extracellular matrix-associated genes differentially expressed between MG and MDMs in BrMs. Rows are *Z*-scored and manually sorted, and columns are ordered by cell type.

(C) Expression of the indicated BrM-specific genes in neutrophils from unmatched healthy blood, *IDH* WT gliomas, and BrMs. Data are represented as mean ± SEM.

See also Figure S6 and Table S6.

adenosine receptor *ADORA2A* (Figure 6C), which attenuates the phenotype of pro-inflammatory neutrophils (Barletta et al., 2012). Furthermore, we found increased expression of *CD177* (Figure 6C), a cell surface receptor that modulates neutrophil migration and activation and serves as a marker for PR3-positive neutrophils, which, in turn, negatively affect T cell proliferation (Yang et al., 2018). Notably, *MET*, which has been linked to recruitment of immunosuppressive neutrophils in cancer (Glodde et al., 2017), was upregulated in neutrophils in a BrM-specific manner (Figure 6C). In sum, we have uncovered multiple disease-specific alterations of myeloid cells extending beyond BrM-TAMs to neutrophils, which has potential implications for the recruitment and activation of other cell types within the TME, including T cells.

TAMs Are Poised toward an Immunomodulatory Phenotype in BrMs

Although we found a significant accumulation of CD4+ and CD8+ T cells in BrMs versus *IDH* WT gliomas by FCM, this analysis of dissociated tissue samples lacks structural information. We thus performed neighborhood analysis of IF-phenotyped *IDH* WT and BrM tissue sections to elucidate whether there is a spatial relationship between TAMs and CD3+ T cells in BrMs. In *IDH* WT gli-

omas, T-MG and T-MDMs mostly neighbored homotypic cells while lacking T cells in their close vicinity (Figures 7A, 7B, and S7A), possibly reflecting the general T cell sparseness in these tumors. In contrast, both TAM populations neighbored T cells far more frequently in BrMs, indicating the potential for interaction (Figures 7A, 7B, and S7A).

We thus investigated the T cell activation state in BrMs in relation to unmatched healthy donor blood and also juxtaposed them to the corresponding populations from *IDH* WT gliomas. Compared with controls, CD4+ T cells from BrM showed evidence of a hyporesponsive, anergic phenotype (Figure 7C), whereas CD8+ T cells exhibited an exhaustion signature (Figure 7D), which usually occurs upon chronic activation, resulting in upregulation of inhibitory receptors. These defective T cell states can be caused by aberrant activation or T cell inhibition by tumor cells and antigen-presenting cells in the TME and are a major obstacle in treating cancers.

To delineate putative mechanisms in the BrM TME that may drive these alterations, we probed the RNA-seq data from CD45− cells, TAMs, and T cells (Figure 7E) for expression of activating and inhibitory immunomodulatory signals (Wei et al., 2018). This revealed upregulation of various canonical T cell

A Glioma *IDH* wt — BrM

Immunofluorescence: DAPI, CD45, CD68/P2RY12, CD49D, CD3

Cell type quantification: Non-immune, MG, MDM, CD3⁺, CD45⁺ other

Glioma *IDH* wt: 31.8%, 50.9%, 03.6%, 13.6%
BrM: 17.1%, 24.3%, 15.8%, 42.8%

B Glioma *IDH* wt — BrM

n neighbors per cell type (MG / MDM), Proportion of neighbor

CD3⁺ T cells, MG, MDM, CD45⁺ other

C CD4⁺ T cells BrM vs. reference
"Safford T lymphocyte anergy"
NES=2.04, p-adjust<0.005

Enrichment score vs. Rank

D CD8⁺ T cells BrM vs. reference
GSE9650 "Effector vs. exhausted CD8 T cell down"
NES=1.44, p-adjust=0.002

Enrichment score vs. Rank

E Heatmap

Glioma *IDH* wt / BrM / BrM vs. Non-tum./Ref. / BrM vs. Glioma *IDH* wt

APC T cell activation:
TNFSF4 (OX40LG), CD80, TNFSF15, ICOSLG (B7RP1), CD40, CD86, TNFSF18

APC T cell inhibition:
PDCD1LG2 (PD–L2), LGALS9 (Galectin–9), BTNL2, HHLA2, CD276 (B7–H3), VTCN1 (B7–H4), CD274 (PD–L1)

APC inhibition:
CD200, CD200R1

T cell activation:
CD70, CD244, CD48, CD40LG, CD44

T cell co-activation:
CD27, ICOS, TNFRSF18 (GITR), TNFRSF4 (OX40), TNFRSF9 (4–1BB), TNFRSF14 (HVEM), CD28, TNFSF9 (CD137L), TNFSF14 (LIGHT), TMIGD2

T cell inhibition:
LAG3, TNFRSF8 (CD30), CTLA4, TIGIT, PDCD1 (PD1), HAVCR2 (TIM–3), BTLA, ADORA2A, TNFRSF25, LAIR1, CD160

Metabolic escape:
IDO1, IDO2

Columns: CD45⁻, MG, MDM, CD4⁺, CD8⁺

Scaled Expr.: max → min
Not detected
log2(fc): 7.5 → -2.5

F Corr. expr. to CD4⁺ %CD45⁺ vs. Module membership

LILRB3, LILRB2, CD52, CNN2, CD300E, BST1

G Expression level, Primary tumor vs. BrM

CNN2 ***, BST1 ***, CD300E ****
LILRB2 ****, LILRB3 ****, CD52 ***

(legend on next page)

activators and co-activators but also mediators of inhibition in T cells (*PDCD1/PD1*, *CD28*, and *CTLA4*), whereas T cell-inhibiting and activating signals were detected in both TAM populations (*CD274/PD-L1* and *PDCD1LG*2/*PD-L2*). Notably, we found an upregulation of *CD80*, which has diverse roles in T cell activation because it heterodimerizes with CD274, provides co-stimulatory signals to T cells via CD28 and exerts inhibitory effects via interaction with CTLA4 (Zhao et al., 2019), in both TAM populations compared with their normal references and *IDH* WT tumor populations (Figure 7E). The potential contribution of TAMs to metabolic immune evasion is also suggested by high expression of *IDO1* and *IDO2* (Zhai et al., 2018) in BrM (Figure 7E).

We investigated additional immunomodulatory mediators using weighted gene correlation network analysis (WGCNA; Langfelder and Horvath, 2008) and correlated the resulting expression patterns with paired FCM abundance of CD4$^+$ and CD8$^+$ cells in a disease- and cell-type-specific manner. We identified 15 unique co-expression modules showing significant correlation (p < 0.05) of their eigengenes (i.e., the first PC of the module expression data) with any of the provided sample traits (Figure S7B). Among these, the "brown" WGCNA module correlated with a specific BrM-MDM annotation and CD4$^+$ T cell abundance. ORA of this module revealed signals for pathways such as coagulation and ECM modulation (Figure S7C) that affect the availability and activity of growth factors and cytokines within the TME (Mohan et al., 2020). We ranked genes by module membership strength and correlation with CD4$^+$ T cell abundance, which identified several factors with opposing immunomodulatory functions (Figure 7F). Although the receptors *CD300E* and *BST1* promote monocyte motility and survival (Isobe et al., 2018; Ortolan et al., 2019), we also detected effectors of immunosuppression, such as the actin-associated regulatory protein *CNN2*, which negatively regulates macrophage motility and phagocytic activity (Huang et al., 2008). The leukocyte immunoglobulin-like receptor subfamily B members LILRB2 and LILRB3, which attenuate myeloid cell activation (van der Touw et al., 2017), are also highly ranked genes within this module. Interestingly, *LILRB2* has been identified as a novel myeloid immune checkpoint that limits antitumor immunity (Chen et al., 2018). We also found evidence of effects on T cells; *CD52*, which, in its soluble form, inhibits T cell function, was among the BrM-

MDM module genes. The notion that BrM-MDMs undergo disease-specific alterations distinct from the primary extracranial tumor is supported by upregulation of these genes (Figure 7G) in our analysis of an external cohort of BrM samples compared with their matched primary tumor tissue (Vareslija et al., 2019).

DISCUSSION

Brain tumors, including glioblastoma and BrMs, confer some of the poorest prognoses for patients with cancer, with survival rates often measured in just months. Given the current dearth of effective therapeutic options for these patients and the modest effects of the various immunotherapies evaluated to date, it is of critical urgency to identify novel targets for future clinical evaluation. One potentially rich source of therapeutic targets is the TME. However, even though the TME is now widely accepted as an important regulator of cancer progression and therapeutic response, our knowledge of the brain TME is restricted to individual brain tumor types or cellular compartments and lacks comprehensive and integrative analysis.

In this study, we leveraged a diverse panel of analyses to deeply interrogate the immune landscape of primary and metastatic brain cancers. Through integration of multiparameter FCM analyses, RNA-seq data, TME cell culture assays, protein arrays, and spatial tissue characterization, we uncovered critical insights into the composition and transcriptomes of the most abundant immune cell populations in patient samples from *IDH* mut and WT gliomas and BrMs originating from distinct extracranial primary tumors.

By exploring the broad immune landscape, we uncovered several pronounced differences between gliomas and BrMs when directly compared side by side. In brain tumors, TAMs are composed of tissue-resident MG and recruited MDMs, and we found a significant shift in the ratio of MG to MDMs between *IDH* mut and *IDH* WT gliomas. Additionally, gliomas contain an abundance of TAMs, whereas T cells were much fewer, particularly in *IDH* mut tumors. This confirms the notion that gliomas are immunologically cold tumors (Jackson et al., 2019). Although T cell sequestration in the bone marrow has been observed in glioma mouse models and following intracranial implantation of brain-extrinsic tumors (Chongsathidkiet et al., 2018), our clinical

---

Figure 7. TAMs Have a Wide Range of Immunomodulatory Functions in BrMs

(A) Representative IF images and corresponding cell type identification of non-immune cells (CD45$^-$), MG (CD45$^+$, P2RY12/CD68$^+$, CD49D$^-$), MDMs (CD45$^+$, P2RY12/CD68$^+$, CD49D$^+$), CD3$^+$ (CD45$^+$, P2RY12/CD68$^-$, CD49D$^{-/+}$, CD3$^+$) and CD45$^+$ other cells (CD45$^+$, P2RY12/CD68$^-$, CD49D$^{-/+}$, CD3$^-$) in *IDH* WT gliomas and BrMs. Scale bars, 50 μm. Insets show quantifications per FOV.

(B) Neighborhood analyses of *IDH* WT glioma and BrM IF tissue sections. Rows show the mean proportion of each neighboring cell type per frequency of observed n$_{neighbors}$ in the vicinity of MG or MDMs (n$_{IDH\ WT}$ = 9, n$_{BrMs}$ = 13).

(C and D) Gene set enrichment analysis (GSEA) of a T cell anergy gene set in CD4$^+$ T cells (C) and a T cell exhaustion gene set in CD8$^+$ T cells (D) from the MSigDB C2 collection.

(E) Gene expression heatmap of antigen-presenting cell (APC) and T cell activating and inhibitory signaling mediators (left panels, scaled to the expression range of variance-stabilized counts across all cell types in *IDH* WT glioma and BrMs) and corresponding fold changes (right panels, BrMs versus non-tumor/reference and *IDH* WT glioma versus BrMs, absolute log2(fold change) > 1, adjusted p value < 0.05) in CD45$^-$ MG and MDMs and CD4$^+$ and CD8$^+$ T cells in *IDH* WT gliomas and BrMs. Gray tiles indicate expression below the threshold (normalized counts < 10); white tiles correspond to a non-significant fold change.

(F) Scatterplot of module membership (correlation of expression to the module eigengene) and gene significance (correlation of expression to CD4$^+$ T cell abundance) of genes from the BrM-MDM-related gene co-expression network. Highly connected genes with immunomodulatory functions are annotated.

(G) Expression of the indicated genes in matched bulk primary breast cancer and BrM tissues using the Vareslija et al. (2019) dataset (Wilcoxon signed-rank test: ***p < 0.001, ****p < 0.0001).

See also Figure S7.

BrM samples showed pronounced accumulation of lymphocytes and neutrophils. This indicates that tumors that arise within the brain indeed shape their TME differently than cancers that metastasize from extracranial sites. Moreover, when exploring BrMs that originate from distinct primary tumors, there were additional differences; for example, in melanoma BrM samples, the combined abundance of CD4$^+$ and CD8$^+$ T cells represented the major immune compartment, whereas breast BrM samples showed the highest neutrophil infiltration. These key differences in the TME landscape, which are evident only when directly juxtaposing different brain malignancies, mirror the efficacy of immunotherapies that show promising efficacy in melanoma patients for controlling BrMs but with very modest effects to date in treating T cell-excluded glioblastoma (Schalper et al., 2019).

We also uncovered complex multifaceted phenotypes for TAMs across different brain tumors that extend beyond their numerical abundance. T-MG and T-MDMs showed distinct transcriptomic profiles and shared expression signatures, which are additionally influenced by the underlying disease type (*IDH* mut versus *IDH* WT glioma versus BrMs). A T-MDM signature derived from *IDH* WT gliomas, consisting of macrophage activation markers, chemokine receptors, and cytokines, proved to also be a predictor of patient survival in *IDH* mut gliomas. Moreover, analyses of T-MDMs indicated that even though these recruited cells have the potential to process and present antigens, and can be located proximally to T cells in BrMs, this potential is evidently not sufficiently utilized within the brain TME. Orthogonal analyses from the diverse panel of experimental assays used in this study reveal additional insights into potential mechanisms of immune suppression. These included our findings that different TAM populations produced pro-inflammatory molecules, negative regulators of myeloid cell activation, factors associated with IPRES, IDO1 and IDO2 immune checkpoint inhibitors, and specific ECM components and proteases that may collectively help sculpt an immune-suppressive niche. Therefore, therapeutic strategies that alter the multifaceted phenotypes of TAMs (Kowal et al., 2019), rather than aiming to simply deplete all of these cells with potentially opposing functions, should be considerably more effective.

Looking beyond TAMs, it will also be critical to assess the roles of neutrophils, particularly in BrMs, where we found them to be highly abundant, because they can act as potent immune-suppressive cells, as indicated by studies of other organs (Coffelt et al., 2016). Given the highly complex and multifaceted immune landscape of brain cancers revealed in this study, it is clear that rational combinations of TME-targeted agents will be critical to avoid the emergence of adaptive resistance, incorporating preclinical studies to help determine optimal combinations (Quail et al., 2016). In sum, this rich resource is available for further interrogation by the research community so that we can work collectively to uncover novel therapeutic strategies that unleash the potential of diverse cells in the TME to combat different brain malignancies.

STAR★METHODS

Detailed methods are provided in the online version of this paper and include the following:

- KEY RESOURCES TABLE
- RESOURCE AVAILABILITY
  - Lead Contact
  - Materials Availability
  - Data and Code Availability
- EXPERIMENTAL MODEL AND SUBJECT DETAILS
- METHOD DETAILS
  - Clinical sample processing, flow cytometry (FCM) and fluorescence activated cell sorting (FACS)
  - Tumor microenvironment-conditioned medium (TME-CM) generation
  - *In vitro* generation of monocyte-derived macrophages (MDM) and TME-CM stimulation
  - RNA isolation, cDNA synthesis and quantitative real-time PCR
  - Immunofluorescence staining and microscopy image acquisition
  - Image analysis and cell type identification
  - Protein isolation and enzyme-linked immunosorbent assay (ELISA)
  - RNA sequencing (RNA-seq)
  - Bioinformatic analysis environment
  - Gene set-centered analyses
  - Deconvolution of Toil-RNA sequencing data
  - Leading edge metagene (LEM) analysis
  - Protein-Protein-Interaction network building
  - Nearest neighbor distance measurements and neighborhood analysis of IF data
  - Cell type abundance estimation in spatial Ivy Glioblastoma Atlas Project (GAP) data
  - Survival analysis of the IDH wt MDM-specific gene signature in gliomas
  - Self-organizing map (SOM) clustering
  - Weighted gene correlation network analysis (WGCNA)
  - Expression analysis of external dataset of matched primary breast cancer and BrMs
  - Plotting and graph generation
- QUANTIFICATION AND STATISTICAL ANALYSIS

AUTHOR CONTRIBUTIONS

DECLARATION OF INTERESTS

REFERENCES

Afik, R., Zigmond, E., Vugman, M., Klepfish, M., Shimshoni, E., Pasmanik-Chor, M., Shenoy, A., Bassat, E., Halpern, Z., Geiger, T., et al. (2016). Tumor macrophages are pivotal constructors of tumor collagenous matrix. J. Exp. Med. 213, 2315–2331.

Aldape, K., Brindle, K.M., Chesler, L., Chopra, R., Gajjar, A., Gilbert, M.R., Gottardo, N., Gutmann, D.H., Hargrave, D., Holland, E.C., et al. (2019). Challenges to curing primary brain tumours. Nat. Rev. Clin. Oncol. 16, 509–520.

Baddeley, A.D., Eysenck, M.W., and Anderson, M.C. (2015). Spatial Point Patterns: Methodology and Applications with R (London: Chapman and Hall/CRC Press).

Barletta, K.E., Ley, K., and Mehrad, B. (2012). Regulation of neutrophil function by adenosine. Arterioscler. Thromb. Vasc. Biol. 32, 856–864.

Bates, D., Machler, M., Bolker, B.M., and Walker, S.C. (2015). Fitting Linear Mixed-Effects Models Using lme4. J. Stat. Softw. 67, 1–48.

Benci, J.L., Xu, B., Qiu, Y., Wu, T.J., Dada, H., Twyman-Saint Victor, C., Cucolo, L., Lee, D.S.M., Pauken, K.E., Huang, A.C., et al. (2016). Tumor Interferon Signaling Regulates a Multigenic Resistance Program to Immune Checkpoint Blockade. Cell 167, 1540–1554.e12.

Bouralexis, S., Findlay, D.M., and Evdokiou, A. (2005). Death to the bad guys: targeting cancer via Apo2L/TRAIL. Apoptosis 10, 35–51.

Bournazos, S., Wang, T.T., and Ravetch, J.V. (2016). The Role and Function of Fcγ Receptors on Myeloid Cells. Microbiol. Spectr. 4 https://doi.org/10.1128/microbiolspec.MCHD-0045-2016.

Bowman, R.L., Klemm, F., Akkari, L., Pyonteck, S.M., Sevenich, L., Quail, D.F., Dhara, S., Simpson, K., Gardner, E.E., Iacobuzio-Donahue, C.A., et al. (2016). Macrophage Ontogeny Underlies Differences in Tumor-Specific Education in Brain Malignancies. Cell Rep. 17, 2445–2459.

Cagney, D.N., Martin, A.M., Catalano, P.J., Redig, A.J., Lin, N.U., Lee, E.Q., Wen, P.Y., Dunn, I.F., Bi, W.L., Weiss, S.E., et al. (2017). Incidence and prognosis of patients with brain metastases at diagnosis of systemic malignancy: a population-based study. Neuro-oncol. 19, 1511–1521.

Ceccarelli, M., Barthel, F.P., Malta, T.M., Sabedot, T.S., Salama, S.R., Murray, B.A., Morozova, O., Newton, Y., Radenbaugh, A., Pagnotta, S.M., et al.; TCGA Research Network (2016). Molecular Profiling Reveals Biologically Discrete Subsets and Pathways of Progression in Diffuse Glioma. Cell 164, 550–563.

Chen, Z., Feng, X., Herting, C.J., Garcia, V.A., Nie, K., Pong, W.W., Rasmussen, R., Dwivedi, B., Seby, S., Wolf, S.A., et al. (2017). Cellular and Molecular Identity of Tumor-Associated Macrophages in Glioblastoma. Cancer Res. 77, 2266–2278.

Chen, H.M., van der Touw, W., Wang, Y.S., Kang, K., Mai, S., Zhang, J., Alsina-Beauchamp, D., Duty, J.A., Mungamuri, S.K., Zhang, B., et al. (2018). Blocking immunoinhibitory receptor LILRB2 reprograms tumor-associated myeloid cells and promotes antitumor immunity. J. Clin. Invest. 128, 5647–5662.

Chongsathidkiet, P., Jackson, C., Koyama, S., Loebel, F., Cui, X., Farber, S.H., Woroniecka, K., Elsamadicy, A.A., Dechant, C.A., Kemeny, H.R., et al. (2018). Sequestration of T cells in bone marrow in the setting of glioblastoma and other intracranial tumors. Nat. Med. 24, 1459–1468.

Coffelt, S.B., Wellenstein, M.D., and de Visser, K.E. (2016). Neutrophils in cancer: neutral no more. Nat. Rev. Cancer 16, 431–446.

Colaprico, A., Silva, T.C., Olsen, C., Garofano, L., Cava, C., Garolini, D., Sabedot, T.S., Malta, T.M., Pagnotta, S.M., Castiglioni, I., et al. (2016). TCGAbiolinks: an R/Bioconductor package for integrative analysis of TCGA data. Nucleic Acids Res. 44, e71.

Cui, Z., Liao, J., Cheong, N., Longoria, C., Cao, G., DeLisser, H.M., and Savani, R.C. (2019). The Receptor for Hyaluronan-Mediated Motility (CD168) promotes inflammation and fibrosis after acute lung injury. Matrix Biol. 78-79, 255–271.

Dobin, A., Davis, C.A., Schlesinger, F., Drenkow, J., Zaleski, C., Jha, S., Batut, P., Chaisson, M., and Gingeras, T.R. (2013). STAR: ultrafast universal RNA-seq aligner. Bioinformatics 29, 15–21.

Filková, M., Haluzík, M., Gay, S., and Senolt, L. (2009). The role of resistin as a regulator of inflammation: Implications for various human pathologies. Clin. Immunol. 133, 157–170.

Friedman, J., Hastie, T., and Tibshirani, R. (2010). Regularization Paths for Generalized Linear Models via Coordinate Descent. J. Stat. Softw. 33, 1–22.

Gabrusiewicz, K., Rodriguez, B., Wei, J., Hashimoto, Y., Healy, L.M., Maiti, S.N., Thomas, G., Zhou, S., Wang, Q., Elakkad, A., et al. (2016). Glioblastoma-infiltrated innate immune cells resemble M0 macrophage phenotype. JCI Insight 1, e85841.

Gaujoux, R., and Seoighe, C. (2010). A flexible R package for nonnegative matrix factorization. BMC Bioinformatics 11, 367.

Georgoudaki, A.M., Prokopec, K.E., Boura, V.F., Hellqvist, E., Sohn, S., Östling, J., Dahan, R., Harris, R.A., Rantalainen, M., Klevebring, D., et al. (2016). Reprogramming Tumor-Associated Macrophages by Antibody Targeting Inhibits Cancer Progression and Metastasis. Cell Rep. 15, 2000–2011.

Glodde, N., Bald, T., van den Boorn-Konijnenberg, D., Nakamura, K., O'Donnell, J.S., Szczepanski, S., Brandes, M., Eickhoff, S., Das, I., Shridhar, N., et al. (2017). Reactive Neutrophil Responses Dependent on the Receptor Tyrosine Kinase c-MET Limit Cancer Immunotherapy. Immunity 47, 789–802.e9.

Godec, J., Tan, Y., Liberzon, A., Tamayo, P., Bhattacharya, S., Butte, A.J., Mesirov, J.P., and Haining, W.N. (2016). Compendium of Immune Signatures Identifies Conserved and Species-Specific Biology in Response to Inflammation. Immunity 44, 194–206.

GTEx Consortium (2013). The Genotype-Tissue Expression (GTEx) project. Nat. Genet. 45, 580–585.

Gutmann, D.H., and Kettenmann, H. (2019). Microglia/Brain Macrophages as Central Drivers of Brain Tumor Pathobiology. Neuron 104, 442–449.

Hänzelmann, S., Castelo, R., and Guinney, J. (2013). GSVA: gene set variation analysis for microarray and RNA-seq data. BMC Bioinformatics 14, 7.

Hendriks, L.E.L., Henon, C., Auclin, E., Mezquita, L., Ferrara, R., Audigier-Valette, C., Mazieres, J., Lefebvre, C., Rabeau, A., Le Moulec, S., et al. (2019). Outcome of Patients with Non-Small Cell Lung Cancer and Brain Metastases Treated with Checkpoint Inhibitors. J. Thorac. Oncol. 14, 1244–1254.

Huang, Q.Q., Hossain, M.M., Wu, K., Parai, K., Pope, R.M., and Jin, J.P. (2008). Role of H2-calponin in regulating macrophage motility and phagocytosis. J. Biol. Chem. 283, 25887–25899.

Hugo, W., Zaretsky, J.M., Sun, L., Song, C., Moreno, B.H., Hu-Lieskovan, S., Berent-Maoz, B., Pang, J., Chmielowski, B., Cherry, G., et al. (2016). Genomic and Transcriptomic Features of Response to Anti-PD-1 Therapy in Metastatic Melanoma. Cell 165, 35–44.

Isobe, M., Izawa, K., Sugiuchi, M., Sakanishi, T., Kaitani, A., Takamori, A., Maehara, A., Matsukawa, T., Takahashi, M., Yamanishi, Y., et al. (2018). The CD300e molecule in mice is an immune-activating receptor. J. Biol. Chem. 293, 3793–3805.

Jackson, C.M., Choi, J., and Lim, M. (2019). Mechanisms of immunotherapy resistance: lessons from glioblastoma. Nat. Immunol. 20, 1100–1109.

Kai, F., Drain, A.P., and Weaver, V.M. (2019). The Extracellular Matrix Modulates the Metastatic Journey. Dev. Cell *49*, 332–346.

Klemm, F., and Joyce, J.A. (2015). Microenvironmental regulation of therapeutic response in cancer. Trends Cell Biol. *25*, 198–213.

Kobayashi, M., Chung, J.S., Beg, M., Arriaga, Y., Verma, U., Courtney, K., Mansour, J., Haley, B., Khan, S., Horiuchi, Y., et al. (2019). Blocking Monocytic Myeloid-Derived Suppressor Cell Function via Anti-DC-HIL/GPNMB Antibody Restores the *In Vitro* Integrity of T Cells from Cancer Patients. Clin. Cancer Res. *25*, 828–838.

Kowal, J., Kornete, M., and Joyce, J.A. (2019). Re-education of macrophages as a therapeutic strategy in cancer. Immunotherapy *11*, 677–689.

Langfelder, P., and Horvath, S. (2008). WGCNA: an R package for weighted correlation network analysis. BMC Bioinformatics *9*, 559.

Lécuyer, M.A., Saint-Laurent, O., Bourbonnière, L., Larouche, S., Larochelle, C., Michel, L., Charabati, M., Abadier, M., Zandee, S., Haghayegh Jahromi, N., et al. (2017). Dual role of ALCAM in neuroinflammation and blood-brain barrier homeostasis. Proc. Natl. Acad. Sci. USA *114*, E524–E533.

Li, L., Yan, J., Xu, J., Liu, C.Q., Zhen, Z.J., Chen, H.W., Ji, Y., Wu, Z.P., Hu, J.Y., Zheng, L., and Lau, W.Y. (2014). CXCL17 expression predicts poor prognosis and correlates with adverse immune infiltration in hepatocellular carcinoma. PLoS ONE *9*, e110064.

Li, Y., Xie, Y., Hao, J., Liu, J., Ning, Y., Tang, Q., Ma, M., Zhou, H., Guan, S., Zhou, Q., and Lv, X. (2018). ER-localized protein-Herpud1 is a new mediator of IL-4-induced macrophage polarization and migration. Exp. Cell Res. *368*, 167–173.

Liberzon, A., Birger, C., Thorvaldsdóttir, H., Ghandi, M., Mesirov, J.P., and Tamayo, P. (2015). The Molecular Signatures Database (MSigDB) hallmark gene set collection. Cell Syst. *1*, 417–425.

Lim, M., Xia, Y., Bettegowda, C., and Weller, M. (2018). Current state of immunotherapy for glioblastoma. Nat. Rev. Clin. Oncol. *15*, 422–442.

Liu, Q., Johnson, E.M., Lam, R.K., Wang, Q., Ye, B.H., Wilson, E.N., Minhas, P.S., Liu, L., Swarovski, M.S., Tran, S., et al. (2019). Peripheral TREM1 responses to brain and intestinal immunogens amplify stroke severity. Nat. Immunol. *20*, 1023–1034.

Löffler-Wirth, H., Kalcher, M., and Binder, H. (2015). oposSOM: R-package for high-dimensional portraying of genome-wide expression landscapes on bioconductor. Bioinformatics *31*, 3225–3227.

Long, G.V., Atkinson, V., Lo, S., Sandhu, S., Guminski, A.D., Brown, M.P., Wilmott, J.S., Edwards, J., Gonzalez, M., Scolyer, R.A., et al. (2018). Combination nivolumab and ipilimumab or nivolumab alone in melanoma brain metastases: a multicentre randomised phase 2 study. Lancet Oncol. *19*, 672–681.

Love, M.I., Huber, W., and Anders, S. (2014). Moderated estimation of fold change and dispersion for RNA-seq data with DESeq2. Genome Biol. *15*, 550.

Mantovani, A., Marchesi, F., Malesci, A., Laghi, L., and Allavena, P. (2017). Tumour-associated macrophages as treatment targets in oncology. Nat. Rev. Clin. Oncol. *14*, 399–416.

Meng, X., Duan, C., Pang, H., Chen, Q., Han, B., Zha, C., Dinislam, M., Wu, P., Li, Z., Zhao, S., et al. (2019). DNA damage repair alterations modulate M2 polarization of microglia to remodel the tumor microenvironment via the p53-mediated MDK expression in glioma. EBioMedicine *41*, 185–199.

Mohan, V., Das, A., and Sagi, I. (2020). Emerging roles of ECM remodeling processes in cancer. Semin. Cancer Biol. *62*, 192–200.

Morianos, I., Papadopoulou, G., Semitekolou, M., and Xanthou, G. (2019). Activin-A in the regulation of immunity in health and disease. J. Autoimmun. *104*, 102314.

Müller, S., Kohanbash, G., Liu, S.J., Alvarado, B., Carrera, D., Bhaduri, A., Watchmaker, P.B., Yagnik, G., Di Lullo, E., Malatesta, M., et al. (2017). Single-cell profiling of human gliomas reveals macrophage ontogeny as a basis for regional differences in macrophage activation in the tumor microenvironment. Genome Biol. *18*, 234.

Murray, P.J., Allen, J.E., Biswas, S.K., Fisher, E.A., Gilroy, D.W., Goerdt, S., Gordon, S., Hamilton, J.A., Ivashkiv, L.B., Lawrence, T., et al. (2014). Macrophage activation and polarization: nomenclature and experimental guidelines. Immunity *41*, 14–20.

Mushtaq, M.U., Papadas, A., Pagenkopf, A., Flietner, E., Morrow, Z., Chaudhary, S.G., and Asimakopoulos, F. (2018). Tumor matrix remodeling and novel immunotherapies: the promise of matrix-derived immune biomarkers. J. Immunother. Cancer *6*, 65.

Noy, R., and Pollard, J.W. (2014). Tumor-associated macrophages: from mechanisms to therapy. Immunity *41*, 49–61.

Olson, O.C., and Joyce, J.A. (2015). Cysteine cathepsin proteases: regulators of cancer progression and therapeutic response. Nat. Rev. Cancer *15*, 712–729.

Ortolan, E., Augeri, S., Fissolo, G., Musso, I., and Funaro, A. (2019). CD157: From immunoregulatory protein to potential therapeutic target. Immunol. Lett. *205*, 59–64.

Puchalski, R.B., Shah, N., Miller, J., Dalley, R., Nomura, S.R., Yoon, J.G., Smith, K.A., Lankerovich, M., Bertagnolli, D., Bickley, K., et al. (2018). An anatomic transcriptional atlas of human glioblastoma. Science *360*, 660–663.

Pyonteck, S.M., Akkari, L., Schuhmacher, A.J., Bowman, R.L., Sevenich, L., Quail, D.F., Olson, O.C., Quick, M.L., Huse, J.T., Teijeiro, V., et al. (2013). CSF-1R inhibition alters macrophage polarization and blocks glioma progression. Nat. Med. *19*, 1264–1272.

Qiao, S., Qian, Y., Xu, G., Luo, Q., and Zhang, Z. (2019). Long-term characterization of activated microglia/macrophages facilitating the development of experimental brain metastasis through intravital microscopic imaging. J. Neuroinflammation *16*, 4.

Quail, D.F., and Joyce, J.A. (2017). The Microenvironmental Landscape of Brain Tumors. Cancer Cell *31*, 326–341.

Quail, D.F., Bowman, R.L., Akkari, L., Quick, M.L., Schuhmacher, A.J., Huse, J.T., Holland, E.C., Sutton, J.C., and Joyce, J.A. (2016). The tumor microenvironment underlies acquired resistance to CSF-1R inhibition in gliomas. Science *352*, aad3018.

R Core Team (2018). R: A Language and Environment for Statistical Computing (R Foundation for Statistical Computing).

Racle, J., de Jonge, K., Baumgaertner, P., Speiser, D.E., and Gfeller, D. (2017). Simultaneous enumeration of cancer and immune cell types from bulk tumor gene expression data. eLife *6*, e26476.

Rau, A., Gallopin, M., Celeux, G., and Jaffrézic, F. (2013). Data-based filtering for replicated high-throughput transcriptome sequencing experiments. Bioinformatics *29*, 2146–2152.

Richards, J., Gabunia, K., Kelemen, S.E., Kako, F., Choi, E.T., and Autieri, M.V. (2015). Interleukin-19 increases angiogenesis in ischemic hind limbs by direct effects on both endothelial cells and macrophage polarization. J. Mol. Cell. Cardiol. *79*, 21–31.

Ripoll, V.M., Irvine, K.M., Ravasi, T., Sweet, M.J., and Hume, D.A. (2007). Gpnmb is induced in macrophages by IFN-gamma and lipopolysaccharide and acts as a feedback regulator of proinflammatory responses. J. Immunol. *178*, 6557–6566.

Robinson, J.T., Thorvaldsdóttir, H., Wenger, A.M., Zehir, A., and Mesirov, J.P. (2017). Variant Review with the Integrative Genomics Viewer. Cancer Res. *77*, e31–e34.

Rodón, L., Gonzàlez-Juncà, A., Inda, Mdel.M., Sala-Hojman, A., Martínez-Sáez, E., and Seoane, J. (2014). Active CREB1 promotes a malignant TGFβ2 autocrine loop in glioblastoma. Cancer Discov. *4*, 1230–1241.

Sankowski, R., Böttcher, C., Masuda, T., Geirsdottir, L., Sagar, Sindram, E., Seredenina, T., Muhs, A., Scheiwe, C., Shah, M.J., et al. (2019). Mapping microglia states in the human brain through the integration of high-dimensional techniques. Nat. Neurosci. *22*, 2098–2110.

Santana Carrero, R.M., Beceren-Braun, F., Rivas, S.C., Hegde, S.M., Gangadharan, A., Plote, D., Pham, G., Anthony, S.M., and Schluns, K.S. (2019). IL-15 is a component of the inflammatory milieu in the tumor microenvironment promoting antitumor responses. Proc. Natl. Acad. Sci. USA *116*, 599–608.

Schalper, K.A., Rodriguez-Ruiz, M.E., Diez-Valle, R., López-Janeiro, A., Porciuncula, A., Idoate, M.A., Inogés, S., de Andrea, C., López-Diaz de Cerio,

A., Tejada, S., et al. (2019). Neoadjuvant nivolumab modifies the tumor immune microenvironment in resectable glioblastoma. Nat. Med. 25, 470–476.

Stupp, R., Mason, W.P., van den Bent, M.J., Weller, M., Fisher, B., Taphoorn, M.J., Belanger, K., Brandes, A.A., Marosi, C., Bogdahn, U., et al.; European Organisation for Research and Treatment of Cancer Brain Tumor and Radiotherapy Groups; National Cancer Institute of Canada Clinical Trials Group (2005). Radiotherapy plus concomitant and adjuvant temozolomide for glioblastoma. N. Engl. J. Med. 352, 987–996.

Subramanian, A., Tamayo, P., Mootha, V.K., Mukherjee, S., Ebert, B.L., Gillette, M.A., Paulovich, A., Pomeroy, S.L., Golub, T.R., Lander, E.S., and Mesirov, J.P. (2005). Gene set enrichment analysis: a knowledge-based approach for interpreting genome-wide expression profiles. Proc. Natl. Acad. Sci. USA 102, 15545–15550.

Szklarczyk, D., Morris, J.H., Cook, H., Kuhn, M., Wyder, S., Simonovic, M., Santos, A., Doncheva, N.T., Roth, A., Bork, P., et al. (2017). The STRING database in 2017: quality-controlled protein-protein association networks, made broadly accessible. Nucleic Acids Res. 45 (D1), D362–D368.

Szulzewsky, F., Arora, S., de Witte, L., Ulas, T., Markovic, D., Schultze, J.L., Holland, E.C., Synowitz, M., Wolf, S.A., and Kettenmann, H. (2016). Human glioblastoma-associated microglia/monocytes express a distinct RNA profile compared to human control and murine samples. Glia 64, 1416–1436.

Tawbi, H.A., Forsyth, P.A., Algazi, A., Hamid, O., Hodi, F.S., Moschos, S.J., Khushalani, N.I., Lewis, K., Lao, C.D., Postow, M.A., et al. (2018). Combined Nivolumab and Ipilimumab in Melanoma Metastatic to the Brain. N. Engl. J. Med. 379, 722–730.

Thapa, B., and Lee, K. (2019). Metabolic influence on macrophage polarization and pathogenesis. BMB Rep. 52, 360–372.

Tsukamoto, H., Fujieda, K., Miyashita, A., Fukushima, S., Ikeda, T., Kubo, Y., Senju, S., Ihn, H., Nishimura, Y., and Oshiumi, H. (2018). Combined Blockade of IL6 and PD-1/PD-L1 Signaling Abrogates Mutual Regulation of Their Immunosuppressive Effects in the Tumor Microenvironment. Cancer Res. 78, 5011–5022.

Van, P., Jiang, W., Gottardo, R., and Finak, G. (2018). ggCyto: next generation open-source visualization software for cytometry. Bioinformatics 34, 3951–3953.

van der Touw, W., Chen, H.M., Pan, P.Y., and Chen, S.H. (2017). LILRB receptor-mediated regulation of myeloid cell maturation and function. Cancer Immunol. Immunother. 66, 1079–1087.

Varešlija, D., Priedigkeit, N., Fagan, A., Purcell, S., Cosgrove, N., O'Halloran, P.J., Ward, E., Cocchiglia, S., Hartmaier, R., Castro, C.A., et al. (2019). Transcriptome Characterization of Matched Primary Breast and Brain Metastatic Tumors to Detect Novel Actionable Targets. J. Natl. Cancer Inst. 111, 388–398.

Venteicher, A.S., Tirosh, I., Hebert, C., Yizhak, K., Neftel, C., Filbin, M.G., Hovestadt, V., Escalante, L.E., Shaw, M.L., Rodman, C., et al. (2017). Decoupling genetics, lineages, and microenvironment in IDH-mutant gliomas by single-cell RNA-seq. Science 355, eaai8478.

Vivian, J., Rao, A.A., Nothaft, F.A., Ketchum, C., Armstrong, J., Novak, A., Pfeil, J., Narkizian, J., Deran, A.D., Musselman-Brown, A., et al. (2017). Toil enables reproducible, open source, big biomedical data analyses. Nat. Biotechnol. 35, 314–316.

Wei, S.C., Duffy, C.R., and Allison, J.P. (2018). Fundamental Mechanisms of Immune Checkpoint Blockade Therapy. Cancer Discov. 8, 1069–1086.

Wickham, H. (2016). ggplot2: Elegant Graphics for Data Analysis (Springer).

Xu, P., Zhang, X., Liu, Q., Xie, Y., Shi, X., Chen, J., Li, Y., Guo, H., Sun, R., Hong, Y., et al. (2019). Microglial TREM-1 receptor mediates neuroinflammatory injury via interaction with SYK in experimental ischemic stroke. Cell Death Dis. 10, 555.

Xue, J., Schmidt, S.V., Sander, J., Draffehn, A., Krebs, W., Quester, I., De Nardo, D., Gohel, T.D., Emde, M., Schmidleithner, L., et al. (2014). Transcriptome-based network analysis reveals a spectrum model of human macrophage activation. Immunity 40, 274–288.

Yan, D., Kowal, J., Akkari, L., Schuhmacher, A.J., Huse, J.T., West, B.L., and Joyce, J.A. (2017). Inhibition of colony stimulating factor-1 receptor abrogates microenvironment-mediated therapeutic resistance in gliomas. Oncogene 36, 6049–6058.

Yang, T.H., St John, L.S., Garber, H.R., Kerros, C., Ruisaard, K.E., Clise-Dwyer, K., Alatrash, G., Ma, Q., and Molldrem, J.J. (2018). Membrane-Associated Proteinase 3 on Granulocytes and Acute Myeloid Leukemia Inhibits T Cell Proliferation. J. Immunol. 201, 1389–1399.

Young, M.D., Wakefield, M.J., Smyth, G.K., and Oshlack, A. (2010). Gene ontology analysis for RNA-seq: accounting for selection bias. Genome Biol. 11, R14.

Zaiss, D.M.W., Gause, W.C., Osborne, L.C., and Artis, D. (2015). Emerging functions of amphiregulin in orchestrating immunity, inflammation, and tissue repair. Immunity 42, 216–226.

Zhai, L., Ladomersky, E., Lenzen, A., Nguyen, B., Patel, R., Lauing, K.L., Wu, M., and Wainwright, D.A. (2018). IDO1 in cancer: a Gemini of immune checkpoints. Cell. Mol. Immunol. 15, 447–457.

Zhao, J., Sun, L., and Li, X. (2017). Commanding CNS Invasion: GM-CSF. Immunity 46, 165–167.

Zhao, Y., Lee, C.K., Lin, C.H., Gassen, R.B., Xu, X., Huang, Z., Xiao, C., Bonorino, C., Lu, L.F., Bui, J.D., et al. (2019). PD-L1:CD80 Cis-Heterodimer Triggers the Co-stimulatory Receptor CD28 While Repressing the Inhibitory PD-1 and CTLA-4 Pathways. Immunity 51, 1059–1073.e9.

STAR★METHODS

KEY RESOURCES TABLE

REAGENT or RESOURCE	SOURCE	IDENTIFIER
Antibodies		
FCM: AF700 mouse monoclonal anti-human CD45 (clone HI30)	BioLegend	Cat#304024; RRID:AB_493761
FCM: BV421 rat monoclonal anti-mouse/human CD11B (clone M1/70)	BioLegend	Cat#101251; RRID:AB_2562904
FCM: PE mouse monoclonal anti-human CD66B (clone G10F5)	BioLegend	Cat#305106; RRID:AB_2077857
FCM: AF488 mouse monoclonal anti-human CD14 (clone HCD14)	BioLegend	Cat#325610; RRID:AB_830683
FCM: BUV737 mouse monoclonal anti-human CD16 (clone 3G8)	BD	Cat#612786; RRID:AB_2833077
FCM: APC mouse monoclonal anti-human CD49D (clone 9F10)	BioLegend	Cat#304308; RRID:AB_2130041
FCM: BV605 mouse monoclonal anti-human CD11C (clone 3.9)	BioLegend	Cat#301636; RRID:AB_2563796
FCM: BV711 mouse monoclonal anti-human anti HLA-DR (clone L243)	BioLegend	Cat#307644; RRID:AB_2562913
FCM: PerCP/Cy5.5 mouse monoclonal anti-human CD3 (clone HIT3a)	BioLegend	Cat#300328; RRID:AB_1575008
FCM: BV 650 mouse monoclonal anti-human anti CD4 (clone OKT4)	BioLegend	Cat#317436; RRID:AB_2563050
FCM: PE mouse monoclonal anti-human CD25 (clone BC96)	BioLegend	Cat#302606; RRID:AB_314276
FCM: BV510 mouse monoclonal anti-human CD127 (clone A019D5)	BioLegend	Cat#351332; RRID:AB_2562304
FCM: PE/Cy7 mouse monoclonal anti-human CD8A (clone HIT8a)	BioLegend	Cat#300914; RRID:AB_314118
FCM: BUV563 mouse monoclonal anti-human CD20 (clone 2H7)	BD	Cat#748456
FCM: BUV563 mouse monoclonal anti-human CD19 (clone SJ25C1)	BD	Cat#612916
FCM: PE/Dazzle mouse monoclonal anti-human CD56 (clone HDC56)	BioLegend	Cat#318348; RRID:AB_2563564
FCM: PE mouse monoclonal anti-human P2RY12 (clone S16001E)	BioLegend	Cat#392103; RRID:AB_2716006
FCM: PE/Cy7 Mouse monoclonal anti-human CD68 (clone Y1/82A)	BioLegend	Cat#333816; RRID:AB_2562936
IF: Mouse monoclonal anti-human CD68 (clone KP1), 1:100 dilution	Abcam	Cat#ab955; RRID:AB_307338
IF: Rat monoclonal anti-human CD49D (clone PS/2), 1:100 dilution	Abcam	Cat#ab25247
IF: Rabbit polyclonal anti-human P2RY12, 1:600 dilution	Sigma-Aldrich	Cat#HPA014518; RRID:AB_2669027
IF: Goat polyclonal anti-human CD45, 1:100 dilution	LSBio	Cat#LS-B14248-300
IF: AF488 mouse monoclonal anti-human CD45 (clone HI30), 1:100 dilution	BioLegend	Cat#304019; RRID:AB_493033
IF: AF488 mouse monoclonal anti-human CD3 (clone UCHT1), 1:100 dilution	BioLegend	Cat#300406; RRID:AB_314060
IF: Sheep polyclonal anti-human CD31, 1:200 dilution	R&D	Cat#AF806; RRID:AB_355617
IF: APC rat monoclonal anti Ki-67 (clone SolA15), 1:100 dilution	Thermo Fisher Scientific	Cat#17-5698-82

(Continued on next page)

Continued

REAGENT or RESOURCE	SOURCE	IDENTIFIER
IF: AF555 donkey anti-rabbit IgG 1:1000 dilution	Thermo Fisher Scientific	Cat#A31572, RRID:AB_162543
IF: AF555 donkey anti-mouse IgG, 1:500 dilution	Thermo Fisher Scientific	Cat#A32773; RRID:AB_2762848
IF: AF488 donkey anti-rat IgG, 1:500 dilution	Thermo Fisher Scientific	Cat#A21208; RRID:AB_141709
IF: AF647 donkey anti-rat IgG, 1:500 dilution	abcam	Cat#ab150155; RRID:AB_2813835
IF: DyLight755 donkey anti-goat IgG, 1:500 dilution	Thermo Fisher Scientific	Cat# SA5-10091; RRID:AB_2556671
IF: AF555 donkey anti-sheep IgG, 1:500 dilution	Thermo Fisher Scientific	Cat#A21436; RRID:AB_2535857
Biological Samples		
Non-tumor, glioma and brain metastasis tissue	Centre Hospitalier Universitaire Vaudois, Lausanne, Switzerland	N/A
Non-tumor, glioma and brain metastasis tissue	Memorial Sloan Kettering Cancer Center, New York, NY, USA	N/A
Healthy donor blood	Transfusion Interrégionale Croix-Rouge Suisse, Epalinges, Switzerland	N/A
Healthy donor blood	New York Blood Bank, New York, NY, USA	N/A
Chemicals, Peptides, and Recombinant Proteins		
DMEM-F12 (1:1), GlutaMAX	GIBCO	Cat#31331028
DMEM, high glucose, GlutaMAX, pyruvate	GIBCO	Cat#31966021
Penicillin/Streptomycin	GIBCO	Cat#15140122
Human recombinant CSF-1	R&D Systems	Cat#216-MC-025
Ficoll-Paque Premium	GE	Cat#17-5442-02
Trizol	Thermo Fisher Scientific	Cat#15596018
Trizol LS	Thermo Fisher Scientific	Cat#10296028
Tween 20	Applied Chemicals	Cat#A4974
Triton X-100	Applied Chemicals	Cat#A4975
TNB Blocking Reagent	Perkin Elmer	Cat#FP1020
Fluorescence Mounting Medium	Dako	Cat#S302380
Critical Commercial Assays		
Brain Tumor Dissociation Kit (P)	Miltenyi	Cat#130-095-942
Tumor Dissociation Kit, human	Miltenyi	Cat#130-095-929
Myelin Removal Beads	Miltenyi	Cat#130-096-733
CD14 MicroBeads, human	Miltenyi	Cat#130-050-201
Human TruStain FcX	BioLegend	Cat#422302
ZombieNIR Fixable Viability Kit	BioLegend	Cat#423106
High Capacity cDNA Reverse Transcription Kit	Applied Biosystems	Cat#4368814
TaqMan Universal PCR Master Mix	Applied Biosystems	Cat#4304437
Quantibody Array Q4000 ELISA	Raybiotech	Cat#QAH-CAA-4000-1
Deposited Data		
RNAseq count data	This paper	https://joycelab.shinyapps.io/braintime/
Human reference genome, hg38	Genomics Data Common	https://gdc.cancer.gov/about-data/data-harmonization-and-generation/gdc-reference-files
TCGA LGG and GBM datasets	Genomics Data Common	https://portal.gdc.cancer.gov/
TOIL TGCA TARGET GTEx datasets	Vivian et al., 2017	https://xenabrowser.net/datapages/
Ivy Glioblastoma Atlas Project RNA sequencing fata	Puchalski et al., 2018	https://glioblastoma.alleninstitute.org/static/download.html

(Continued on next page)

Continued

REAGENT or RESOURCE	SOURCE	IDENTIFIER
STRING Protein-Protein-Interaction database, version 10.5	Szklarczyk et al., 2017	https://version-10-5.string-db.org/cgi/download.pl
Molecular Signatures Database gene set collection	Liberzon et al., 2015; Subramanian et al., 2005	https://www.gsea-msigdb.org/gsea/msigdb/
RNA sequencing count matrix from matched breast cancer primaries and brain metastases	Vareslija et al., 2019	https://github.com/npriedig
Oligonucleotides		
See Table S7		N/A
Software and Algorithms		
FlowJo, version 10.4	BD	https://www.flowjo.com/
BBDuk, version 38.12	Joint Genome Institute	https://jgi.doe.gov/data-and-tools/bbtools/
STAR aligner, version 2.5.2b	Dobin et al., 2013	https://github.com/alexdobin/STAR
R environment, version 3.5.0	R Core Team, 2018	https://www.r-project.org/
VIS Image Analysis, version 2019.7	Visiopharm	https://www.visiopharm.com/
Other		
gentleMACS Octo Dissociator	Miltenyi	Cat#130-095-937
gentleMACS C Tubes	Miltenyi	Cat#130-096-334
LS Columns	Miltenyi	Cat#130-042-401
SepMate-50	StemCell	Cat#85450
PermaLife Cell Culture Bags	OriGen Biomedical	Cat#PL30-2G
LSR II flow cytometer	BD	N/A
Fortessa flow cytometer	BD	N/A
FACSAria III, flow cytometer & cell sorter	BD	N/A
Axio Scan.Z1 slide scanner	Zeiss	N/A
QuantStudio 6 Flex	Applied Biosystems	N/A
Omni Tissue Homogenizer (TH)	Omni International	Cat#TH220

RESOURCE AVAILABILITY

Lead Contact

Further information and requests for resources should be directed to the Lead Contact, Johanna Joyce (johanna.joyce@unil.ch).

Materials Availability

This study did not generate new unique reagents.

Data and Code Availability

RNA-seq count expression data generated during this study can be visualized and downloaded at https://joycelab.shinyapps.io/braintime/. Due to patient privacy protection, the raw RNA-seq data will be made available upon request.

EXPERIMENTAL MODEL AND SUBJECT DETAILS

All procedures performed in studies involving human participants were in accordance with the ethical standards of the institutional and/or national research committee and with the 1964 Helsinki declaration and its later amendments or comparable ethical standards.

Informed consent was obtained from all individual participants included in this study. The collection of non-tumor and tumor tissue samples at the Centre Hospitalier Universitaire Vaudois (CHUV, Lausanne, Switzerland) was approved by the Commission cantonale d'éthique de la recherche sur l'être humain (CER-VD, protocol PB 2017-00240, F25 / 99). Sample collection at Memorial Sloan Kettering Cancer Center (MSKCC, New York, NY, USA) was approved by the institutional review board (IRB, protocols #IRB #06-107, #14-230). Non-tumor samples of cerebral cortex tissues were collected at CHUV during medically indicated surgical treatment of

refractory epilepsy patients, and at MSKCC in normal brain distant from the tumor in patients with low-grade glioma or from post-mortem samples collected through the rapid autopsy program with no history of brain malignancy.

Tissue specimens were immediately collected from the operating room and processed as described below. All patient-related data and unique identifiers were removed so that human samples were anonymized before any further processing.

Pathological review and molecular analysis of tumor samples was performed as part of standard clinical care at the respective locations (CHUV or MSKCC). In all glioma samples subjected to RNA sequencing, the *IDH1 and IDH2* mutation status was verified by inspection of the reads from the CD45⁻ population aligning to the *IDH1* and *IDH2* loci with the Integrative Genomics Viewer (IGV; Robinson et al., 2017). For immunofluorescence sections the tumor diagnosis was confirmed independently, for all non-tumor samples, the absence of malignancy was equally confirmed by a pathologist.

Peripheral blood and buffy coats were obtained from the Transfusion Interrégionale, Croix-Rouge Suisse (Epalinges/Lausanne, Switzerland), the New York Blood Center (New York, NY, USA), and healthy donors.

METHOD DETAILS

Clinical sample processing, flow cytometry (FCM) and fluorescence activated cell sorting (FACS)

Tissue specimens were washed in HBSS and macro-dissected under sterile conditions. Parts of the tissue were either immediately frozen by submerging the sample in liquid nitrogen-cooled 2-methyl butane (Sigma-Aldrich) or OCT-embedded (Tissue-Tek) before freezing for subsequent sectioning and immunofluorescence staining. OCT embedding was performed by placing the sample in a freezing mold filled with OCT and then submerging the mold in 2-methyl butane cooled with dry ice.

The remaining tissue was further processed with either the Brain Tumor Dissociation Kit (Miltenyi) for non-tumor tissue and gliomas, or the Tumor Dissociation Kit for BrMs (Miltenyi) using the gentleMACS Octo Dissociator (Miltenyi). Myelin debris in cell suspensions from non-tumor and glioma tissues was removed by incubating the cells with Myelin Removal Beads (Miltenyi) and magnetic-activated cell sorting (MACS) using LS columns (Miltenyi) according to the manufacturer's instructions. All tissue suspensions were filtered through a 40 μm filter and underwent red blood cell lysis (BioLegend). Single cell suspensions were stained with a fixable live-dead stain (Zombie NIR, BioLegend), FC-blocked for 10 min (Human TruStain FcX, BioLegend) and then incubated with direct fluorophore-conjugated antibodies for 20 min at 4°C. All FCM antibodies were titrated in a lot-specific manner. Antibody details are listed in the Key Resources Table. Cells were washed with PBS +2% fetal bovine serum (FBS) +0.5 mM EDTA and stored at 4°C in the dark until FAC-sorting.

All FCM acquisition was completed on either a BD Fortessa or a BD LSR II device (BD), and cell sorting was performed on a FACSAria III (BD) using FACSDiva (BD). Cells were sorted directly into Trizol LS (Thermo Fisher Scientific) and immediately snap frozen with liquid nitrogen. Analysis of FCM data was performed with FlowJo (BD).

Tumor microenvironment-conditioned medium (TME-CM) generation

Single cell suspensions from whole tumor samples were resuspended in DMEM-F12 (1:1) +Glutamax (GIBCO) +10% FBS +1% penicillin/streptomycin (P/S, GIBCO) and adjusted to a concentration of 2×10^6 cells/ml with 2 ml plated into each well of a 6-well plate (TPP). The supernatant of these tissue cultures, containing cancer cells, immune cells etc. from the complex brain TME, was harvested at 24 hours after initial seeding, spun down to remove debris (300 g, 10 min) and stored at −80°C until further use.

In vitro generation of monocyte-derived macrophages (MDM) and TME-CM stimulation

Peripheral blood mononuclear cells were isolated from buffy coats of healthy donors with a Ficoll (GE) gradient using SepMate tubes (StemCell) and monocytes selected by MACsorting with CD14 MicroBeads (Miltenyi). Monocytes were differentiated into macrophages by culture in Teflon-coated bags (OriGen) for 7 days in DMEM +GlutaMAX (GIBCO) +10% FBS +1% P/S with the addition of 10 ng/ml recombinant human CSF-1 (R&D Systems).

Differentiated MDMs were plated at a density of 1×10^6 cells/well of a 6-well plate in DMEM +10% FBS +1% P/S +10 ng/ml CSF-1. After cell attachment, MDMs were cultured in serum free medium for 6 hours before stimulation with TME-CM for 24 hours.

RNA isolation, cDNA synthesis and quantitative real-time PCR

TME-CM-stimulated MDMs were lysed with Trizol (Thermo Fisher Scientific), RNA was purified with Direct-zol columns (Zymo Research), DNase treated and 1.0 μg of RNA was used for cDNA synthesis using the High Capacity cDNA Reverse Transcription Kit (Applied Biosystems). An amount of cDNA equivalent to 5 ng total RNA was used for real-time PCR. For primer and probe details see Table S6. Assays were run in triplicate on a QuantStudio 6 Flex instrument (Applied Biosystems) using the TaqMan Universal PCR Master Mix (Applied Biosystems) and expression was normalized to the average expression of *Ubiquitin C* (*UBC*) and *Ribosomal Protein L19* (*RPL19*) for each sample.

Immunofluorescence staining and microscopy image acquisition

10 μm cryostat sections were thawed, air-dried and fixed with ice-cold 100% methanol for 5 minutes. After rehydration with PBS, sections were washed twice in PBS +0.2% Tween 20 (Applied Chemicals), permeabilized with PBS +0.2% Triton X-100 (Applied Chemicals) for 3 hours and washed again with PBS +0.2% Tween 20. Blocking was performed with PBS +0.5% Tween 20 +1%

TNB Blocking Reagent (Perkin Elmer), followed by incubation with primary antibody in the same buffer overnight at 4°C. Primary antibody information and dilutions are listed in the Key Resources table. Sections were washed with PBS +0.2% Tween 20 before incubation with fluorophore-conjugated secondary antibodies at a dilution of 1:500 in PBS +0.5% Tween 20 +1% TNB Blocking Reagent +1 μg/ml DAPI at room temperature. Directly-conjugated primary antibodies were employed where indicated after an initial round of primary and secondary antibody staining, to avoid potential for cross reactivity. Finally, sections were washed with PBS +0.2% Tween and mounted with Fluorescence Mounting Medium (Dako).

Stained tissue sections were imaged with an Axio Scan.Z1 slide scanner (Zeiss) equipped with a Colibri 7 LED light source (Zeiss) using a Plan-Apochromat 20x/0.8 DIC M27 coverslip-corrected objective (Zeiss). All slides from the same staining panel were digitalized using identical acquisition settings.

Image analysis and cell type identification

Image quantification was performed using the VIS Image Analysis software (Visiopharm). For each staining panel a specific application was created using the software's authoring module. The tissue outline was detected after applying a 21 pixel mean filter. The edges of the derived regions of interest were smoothened with the built-in function "close" and holes in the mask were filled using the "fill holes" command. Aberrant signals resulting from e.g., dust particles, tissue folds or air bubbles were manually excluded from these regions of interest. Nuclear classification was based on the watershed signal of the DAPI staining and filtered by area to exclude incomplete nuclei. The obtained nuclear label was expanded by 5 pixels to capture both nuclear and adjacent cytoplasmic fluorescent signal. Cell types were identified using a hierarchical decision tree with manually set thresholds. Finally, a representation of the cytoplasm was created using the inbuilt growth algorithm with a maximum distance of 15 pixels from the nucleus. Vessel segmentation was performed by creating a separate classifier based on pixel intensity of the CD31 signal. Nuclear classifiers were excluded *a priori* and incorporated in the vessel label only when exceeding the threshold for CD31. Perivascular niches (PVNs) were established by generating an ROI around vessels at a distance of 20 μm. All object-based phenotyping result tables were exported as csv files for further analysis within the R environment.

Protein isolation and enzyme-linked immunosorbent assay (ELISA)

Frozen tissues were weighed and homogenized on ice with an Omni Tissue Homogenizer (Omni International) in 10 μL of RIPA lysis buffer (Thermo Fisher Scientific) +cOmplete Protease Inhibitor (Roche Diagnostics) per mg of tissue. The homogenate was gently agitated on ice for 10 minutes, centrifuged at 10.000 g for 5 minutes at 4°C and the supernatant collected. The protein concentration was determined using a Bradford assay (Bio-Rad) and adjusted to 1 μg/μl. Samples were shipped to Raybiotech (Peachtree Corners) for quantitative analysis with the multiplexed Quantibody Array Q4000 ELISA.

RNA sequencing (RNA-seq)

RNA was isolated by chloroform extraction and isopropanol precipitation. RNA sequencing libraries were generated with the SMART-Seq preparation kit (CloneTech) and fragmented with the Nextera XT kit (Illumina). Paired end, 100 or 150 base pair, and single end, 100 base pair, sequencing was performed by Genewiz (South Plainfield, New Jersey, USA) on an Illumina HiSeq 2500 (Illumina).

Reads were adaptor trimmed and quality clipped using BBDuk (version 38.12; https://sourceforge.net/projects/bbmap/). Trimmed reads were mapped to the Genomic Data Commons (GDC) GRCh38.d1.vd1 reference sequence using the STAR aligner (version 2.5.2b, Dobin et al., 2013) in two-pass mode with parameters corresponding to the GDC RNA-seq alignment workflow. Transcript abundance was estimated using the corresponding GDC reference gtf file. A raw count matrix was produced and differential gene expression was assessed with DESeq2 using an absolute log2 fold change of 1 and a false discovery rate of 0.01 when contrasting to reference samples, and 0.05 for within tumor contrasts (Love et al., 2014).

Bioinformatic analysis environment

All bioinformatic analyses were performed within the R environment (version 3.5.0, R Core Team 2018).

Gene set-centered analyses

The Molecular Signatures Database (MSigDB, version 6.1, Liberzon et al., 2015; Subramanian et al., 2005) was used as the main source for gene set-based analyses.

Over-representation was assessed with the goseq R package (Young et al., 2010) for differentially expressed genes to correct for gene length bias, otherwise the hypergeometric test was employed. For individual samples, gene set enrichment was estimated with the Gene Set Variation Analysis R package (GSVA, Hänzelmann et al., 2013) using the "gsva" function. Gene set enrichment analysis (GSEA) was evaluated with the R package fgsea (https://github.com/ctlab/fgsea) using the maximum likelihood log fold changes determined by DESeq2 as the ranking metric.

Deconvolution of Toil-RNA sequencing data

Toil-processed (Vivian et al., 2017), DESeq2-standardized gene expression data and matching phenotype data from the TCGA and Genotype-Tissue Expression Project (GTEx) databases were downloaded from the UCSC Xena platform and filtered to include only

low-grade glioma "TCGA-LGG" and high-grade "TCGA-GBM" and "frontal cortex" GTEx samples to integrate bulk glioma expression data with unmatched non-tumor samples. MG- and MDM-specific marker genes were derived by identifying differentially expressed genes in these two populations versus all other sorted populations in a pairwise fashion, determining the intersect and ranking the resulting genes by their fold change versus the CD45⁻ population. The 20 highest ranked genes were then used as cell type-specific marker genes. Deconvolution of MG- and MDM-proportions in tumor and non-tumor sample expression data was done with the EPIC R package (Racle et al., 2017) using these marker genes and providing the expression data from the sorted populations as reference profiles. As the exact amount of RNA within the estimated cell types is not known, this parameter was set to 1 when running the deconvolution.

Leading edge metagene (LEM) analysis

To capture biologically meaningful patterns of gene expression within the differentially expressed genes the LEM approach (Godec et al., 2016) was employed: (a) GSEA was performed using the MSigDB C7 collection as described above, (b) the leading edge genes of the significant gene sets were arranged into a genes by gene sets matrix with the shrunken fold changes as the entries, (c) this matrix was clustered using non-negative matrix factorization with the R package NMF (Gaujoux and Seoighe, 2010), (d) genes with a small coefficient in each metagene were filtered based on the 95th quantile of a fitted exponential distribution of the coefficients and (e) each gene with a coefficient above the threshold was assigned to the metagene where it had the highest coefficient.

Protein-Protein-Interaction network building

Version 11.0 of the STRING database (Szklarczyk et al., 2017) was downloaded from the consortium's website and gene identifiers from RNA-seq were mapped to Ensembl Protein IDs using the provided accessory data. The resulting interaction data was filtered to contain only interactions with a high confidence STRING combined score (i.e., > 700). For network layout calculation the combined score was used as an edge weight.

Nearest neighbor distance measurements and neighborhood analysis of IF data

Nearest neighbor distances from MG and MDM to vessels in *IDH* wt glioma samples were calculated using the spatstat R package (Baddeley et al., 2015). Statistical significance was assessed by fitting a mixed effects model with the cell type as the fixed effect, and the clinical sample ID as the random effect using the R package lme4 (Bates et al., 2015).

Neighbors for each individual cell were determined based on their occurrence within a range of 5 μm outside of the radius of the cell (calculated based on the area). This was used to tabulate the number of neighbors and their cell type for each cell within the tissue section.

Cell type abundance estimation in spatial Ivy Glioblastoma Atlas Project (GAP) data

The micro-dissected Ivy GAP (Puchalski et al., 2018) RNA-seq RSEM count data and sample annotation containing anatomical location were downloaded from the Ivy GAP website (https://glioblastoma.alleninstitute.org/static/download.html) and normalized using DESeq2. The relative abundance of cell types was estimated by deriving marker genes through a multinomial logistic regression model on the normalized expression data of the FAC-sorted cell types of interest in *IDH* WT tumors and then computing the GSVA enrichment scores in the Ivy GAP samples.

Survival analysis of the IDH wt MDM-specific gene signature in gliomas

The harmonized TCGA low-grade and high-grade HTSeq hg38 count data and clinical data was accessed from the GDC repository using the TCGAbiolinks R package (Colaprico et al., 2016). Datasets were pre-processed to remove outliers and normalized using the functions provided by TCGAbiolink before merging. Subsequent analyses were performed including only samples where an annotation of the *IDH* mutation status was available. Cell type-specific gene signatures were derived by training a multinomial logistic regression model with an elastic-net penalty to separate between MG and MDMs along *IDH* status with the "glmnet" R package (Friedman et al., 2010). A mean-centered expression matrix of all MG and MDMs expression data in gliomas and BrMs, subset by genes that were upregulated in tumors versus non-tumor tissue or healthy controls, served as the input matrix. The strength of the penalty was determined by a 10-fold cross-validation of the λ parameter. For survival analysis, GSVA enrichment scores of these cell type-specific gene signatures were estimated and used to divide samples into tertiles. Kaplan-Meier survival curves were computed using the "survfit" function. Survival curves were compared with a log-rank test between the individual levels and multivariate Cox regression analysis was performed with the "coxph" function.

Self-organizing map (SOM) clustering

Variance stabilized counts from sorted populations of interest from *IDH* mut, *IDH* WT glioma and BrM samples were filtered with the R package HTSFilter (Rau et al., 2013) to ensure removal of genes with a low, constant expression. The resulting matrix of genes and samples was used as input for the SOM neural network building, which was performed with the oposSOM R package (Löffler-Wirth et al., 2015) with a map space of 50 × 50. To investigate associations between the sample phenotype and the SOM metagenes, the tumor type and cell type were provided as group labels.

Weighted gene correlation network analysis (WGCNA)

The WGCNA (Langfelder and Horvath, 2008) R package was used to identify co-regulated genes associated with a MG- or MDM-BrM phenotype. A variance stabilized, batch-corrected count matrix of MG and MDM samples was filtered with the R package HTSFilter (Rau et al., 2013) yielding input expression data with 15826 genes and 56 samples. WGCNA standard parameters were changed as follows: the soft-thresholding power was raised to 7, the minModuleSize was increased to 50, "bicor" was used to calculate the correlation, the network type was set to "signed hybrid" and a dendrogram cut height of 0.25 was used for module merging. This yielded 20 modules whose eigengene, i.e., the first principal component, was tested for correlation to the provided sample information, i.e., tumor- and cell-type and abundance as determined by FCM.

Expression analysis of external dataset of matched primary breast cancer and BrMs

RNA-seq raw count data from patient-matched primary breast tumors and corresponding BrMs (Vareslija et al., 2019) were downloaded (https://github.com/npriedig/jnci_2018) and transformed using DESeq2. The statistical significance of gene expression changes between primary tumors and BrMs was assessed with a two-tailed Wilcoxon signed-rank test on the variance-stabilized counts.

Plotting and graph generation

Plots were created using the ggplot2 R package (Wickham, 2016) and the ggpubr (https://cran.r-project.org/web/packages/ggpubr/), survminer (https://cran.r-project.org/web/packages/survminer/), ggraph (https://cran.r-project.org/web/packages/ggraph/) and ggcyto extensions (Van et al., 2018). Annotated heatmaps were drawn with the pheatmap R package (https://cran.r-project.org/web/packages/pheatmap/).

QUANTIFICATION AND STATISTICAL ANALYSIS

Summary data are presented as mean ± standard error of the mean (SEM) or Tukey boxplots using "ggplot2." Numerical data was analyzed using the statistical tests noted within the corresponding sections of the article. Hierarchical clustering was performed using Ward's method with 1-Pearson correlation coefficient as the distance metric unless noted otherwise. P values were annotated as follows: * < 0.05, ** < 0.01, *** < 0.001, **** < 0.0001, ns > 0.05.

Supplemental Figures

A

B
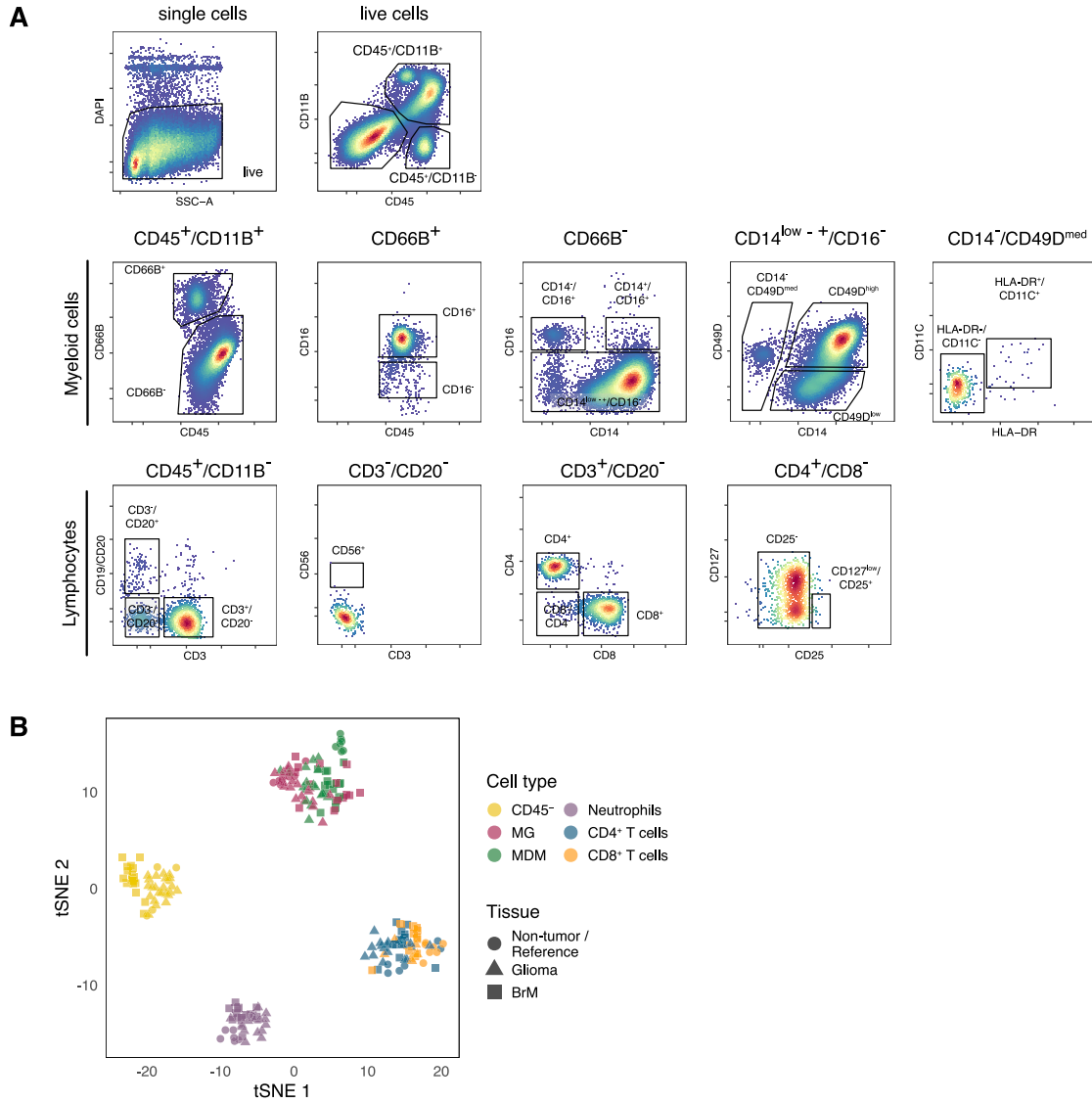
Figure S1. FACS of Cell Populations and RNA-Seq, Related to Figure 1

(A) Flow cytometry (FCM) plots illustrating the gating strategy employed during FAC-sorting of immune cell populations in non-tumor and tumor tissue (for cell type markers, see Table S2). (B) tSNE plot of gene expression data (500 most variable genes) from all sorted cell populations (n = 226) across the complete clinical cohort (MG = microglia, MDM = monocyte-derived macrophages, reference = unmatched healthy blood and *in vitro* generated MDMs).
See also Table S2.
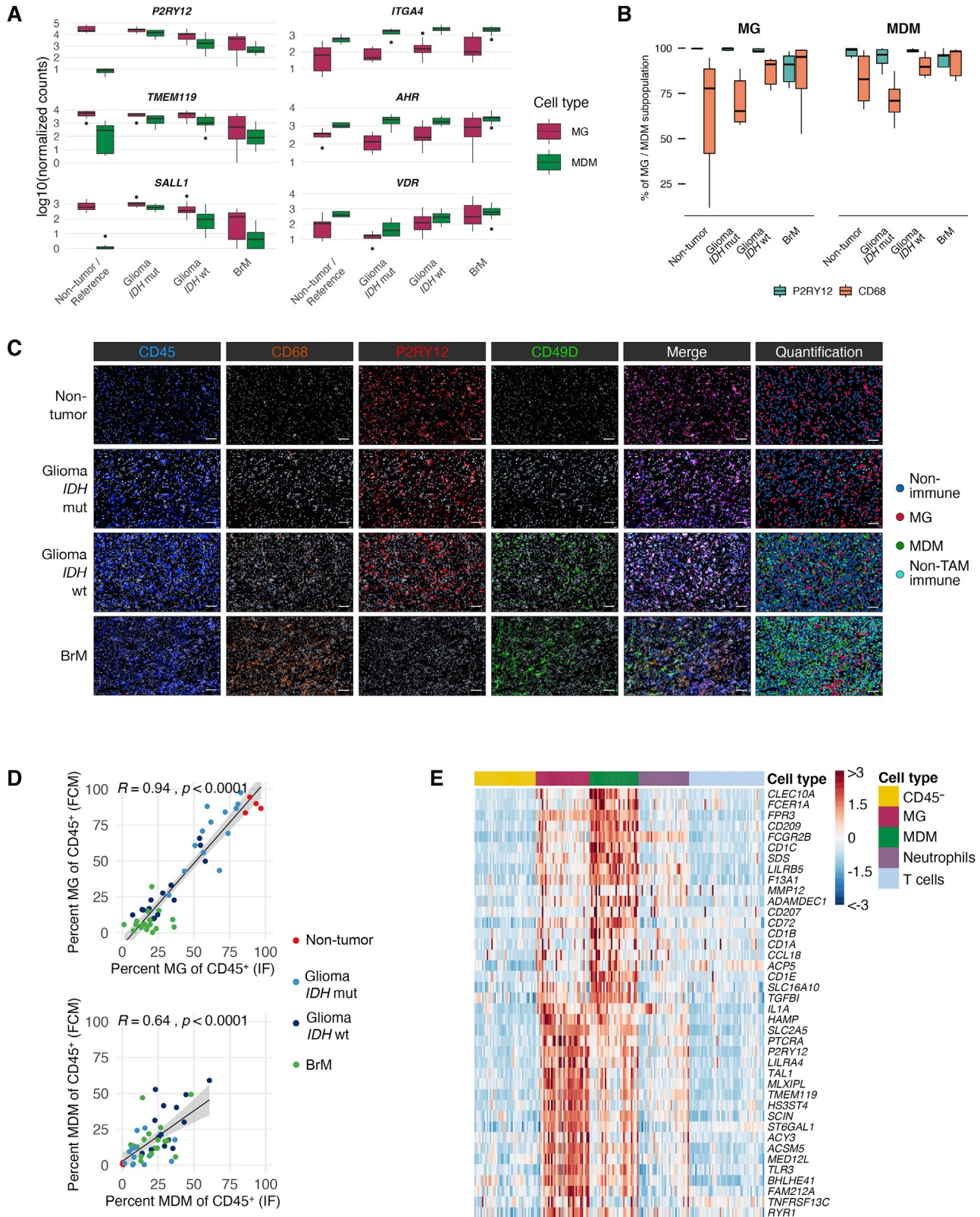
(A) Normalized counts (log10 transformed) of MG and MDM marker genes in sorted CD49D^{low} MG and CD49D^{high} MDM populations across both non-tumor and tumor tissues (reference = healthy donor *in vitro* generated MDMs). (B) Percentage of CD49D^{low} MG and CD49D^{high} MDMs positive for P2RY12 and CD68 as determined by FCM in relation to the total number of MG/MDMs in non-tumor (n = 8) and tumor tissue (n$_{IDH\ mut}$ = 6, n$_{IDH\ WT}$ = 6, n$_{BrM}$ = 9). (C) Single channel and merged immunofluorescence (IF) images of CD45, CD68, P2RY12 and CD49D stainings which were employed to delineate MG and MDMs. The last column shows the resulting Visiopharm cell type assignments for quantitative analyses (MG (CD45^{+}, P2RY12^{+}/CD68^{+}, CD49D^{-}), MDM (CD45^{+}, P2RY12^{+}/CD68^{+}, CD49D^{+}), non-immune cells (CD45^{-}) and non-TAM-immune cells (CD45^{+}, P2RY12^{-}/CD68^{-}, CD49D$^{-/+}$). Scale bars represent 100µm. (D) Scatterplots of the abundance of MG and MDMs as determined by IF versus FCM in non-tumor (n = 4) and tumor tissues (n$_{IDH\ mut}$ = 13, n$_{IDH\ WT}$ = 14, n$_{BrM}$ = 18) processed independently from the same individual samples. Pearson's correlation coefficient and significance are indicated at the top of each plot. (E) Heatmap of human MG- and MDM-specific gene set expression used for deconvolution across FAC-sorted population samples from all disease types.
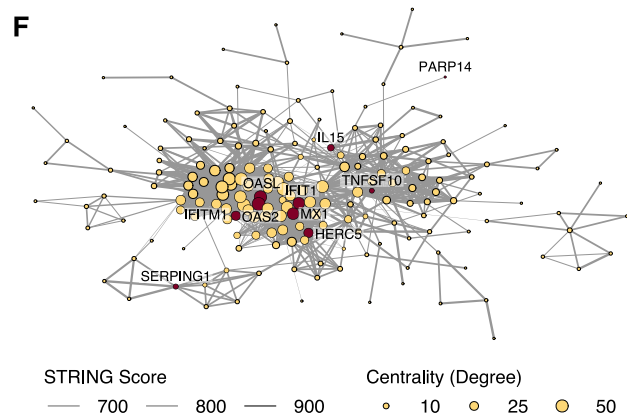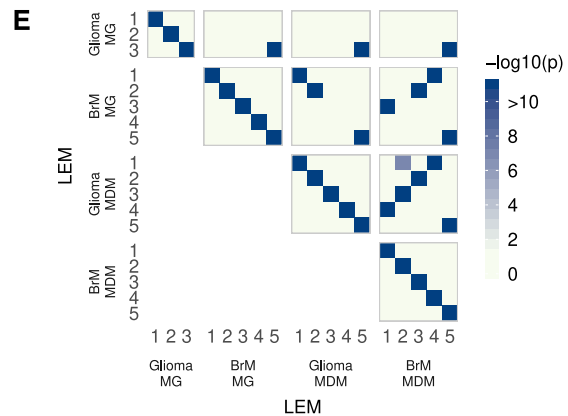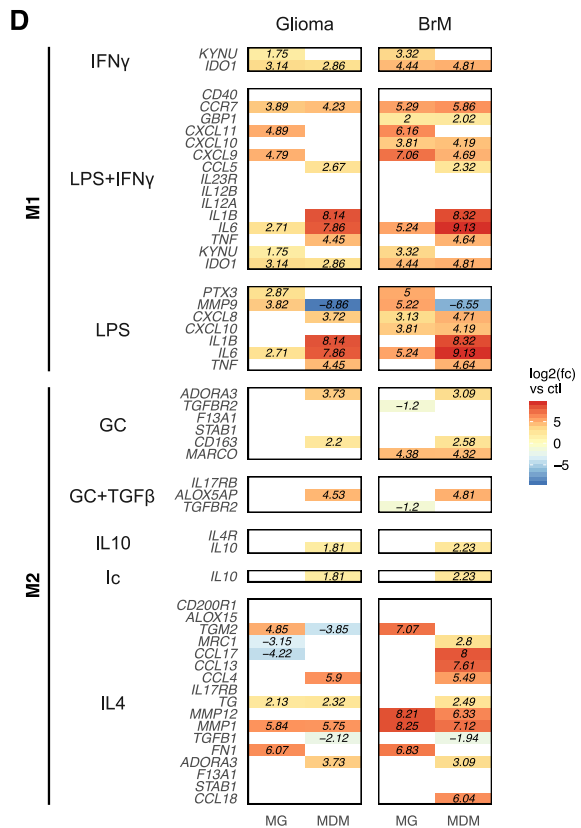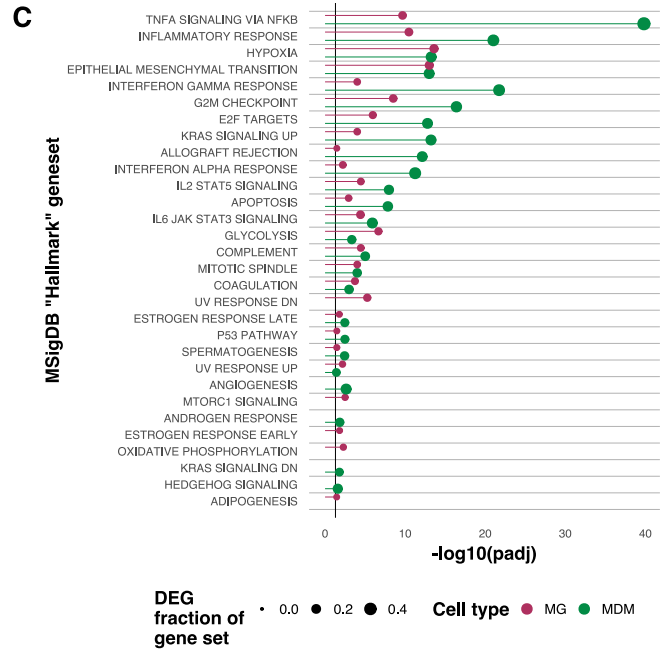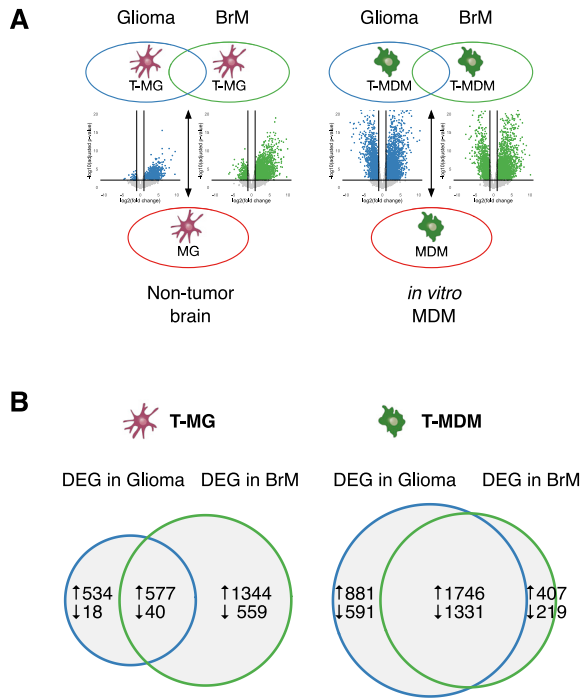
Figure S3. Analysis of DEGs and TAM Activation Patterns, Related to Figure 3

(A) Summary of contrasts applied when performing differential gene expression (DEG) analysis in MG and MDMs in gliomas (regardless of *IDH* status) and BrMs (from all primaries) in comparison to normal controls (non-tumor brain MG and *in vitro* differentiated MDMs respectively) with the corresponding log2(fold-change) versus -log10(adjusted p value) volcano plots. (B) Euler plot of the number of differentially expressed genes (DEG, log2(fc) > 1, p.adj < 0.01) that overlap in MG and MDMs as shown in (A). (C) Molecular Signatures Database (MSigDB) "Hallmark" gene set collection overrepresentation analysis (ORA) in genes upregulated in both gliomas and BrMs versus non-tumor brain tissue or healthy donors in MDMs and MG in MDMs and MG. Dot sizes reflect the fraction of gene set members found within the analyzed DEGs, and dot color indicates cell type. (D) Heatmap of fold changes of macrophage M1 and M2 polarization marker genes (absolute log2(fc) > 1, p.adj < 0.05) in MDMs and MG in gliomas and BrMs. Blank tiles indicate the lack of significant fold change. Genes are annotated with their canonical stimuli and the associated polarization phenotype. (GC = glucocorticoid, Ic = immune complexes, IFNγ = Interferon gamma, IL10 = interleukin 10, IL4 = interleukin 4, LPS = lipopolysaccharide, TGFβ = transforming growth factor beta). (E) Overlap between leading edge metagenes (LEMs) in MG and MDMs in gliomas and BrMs. Tile fill color indicates significance of overlap determined by hypergeometric testing (-log10(p.adj)). (F) String-DB protein-protein-interaction network of the intersect from IFN Type-1 group 2 modules from LEMs "BrM-MG 1," "Glioma MDM 1" and "BrM-MDM 4." Genes selected for validation through qRT-PCR are highlighted in red (corresponding data shown in Figure 3E). Node size indicates the centrality, while edge width corresponds to the String-DB interaction score (only scores > 700, i.e., with a high degree of confidence have been included).
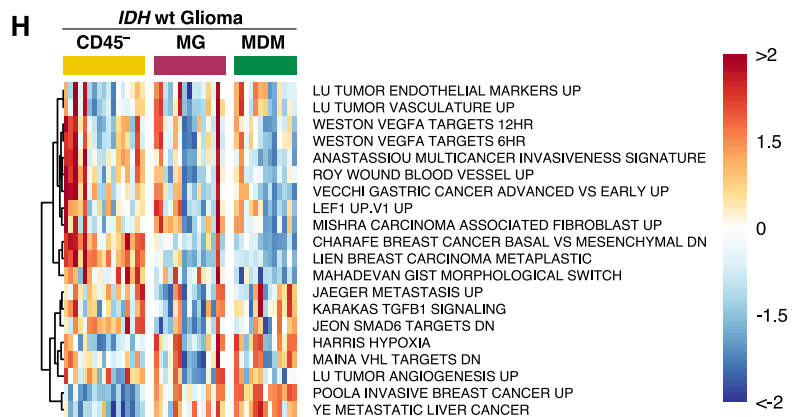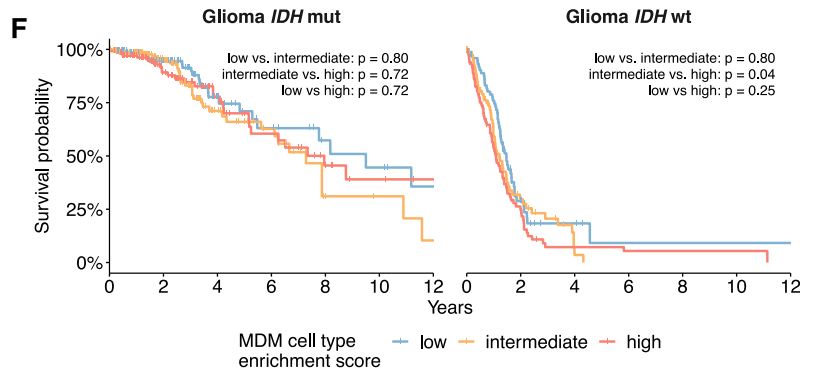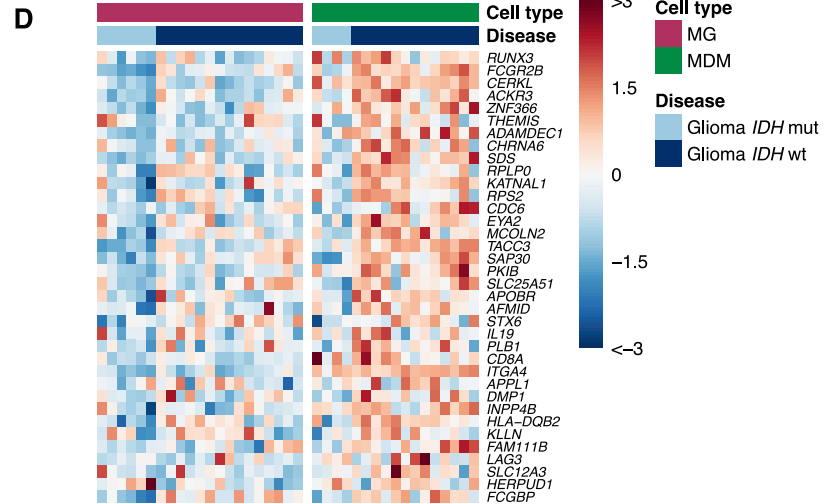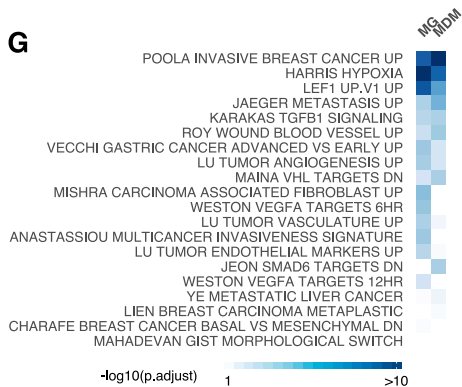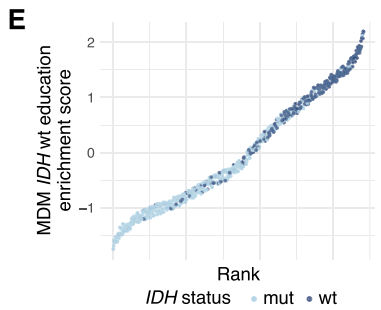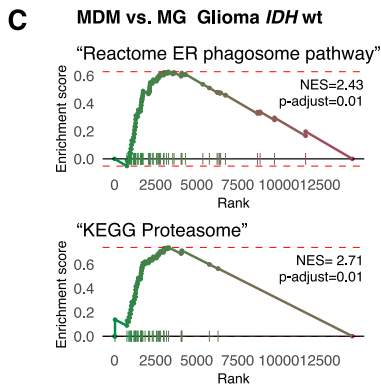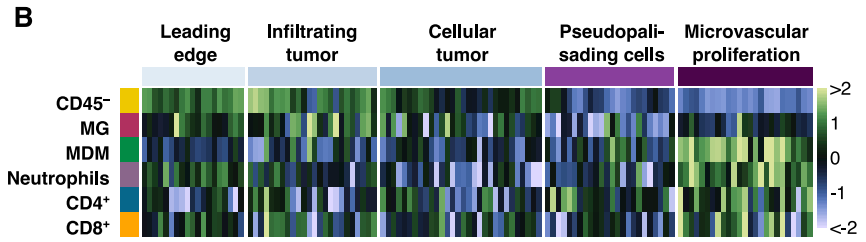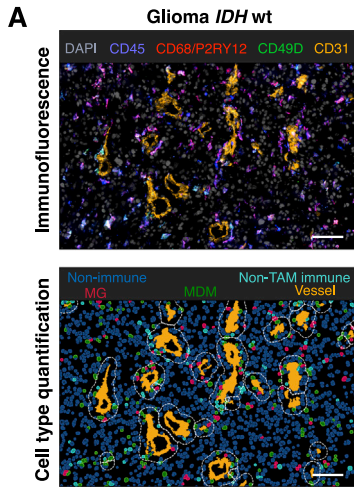
Figure S4. *IDH* WT-Specific Alterations in TAMs, Related to Figure 4

(A) Representative IF image and cell type quantification below of non-immune cells (CD45⁻), non-TAM immune cells (CD45⁺, P2RY12/CD68⁻, CD49D⁺/⁻), MG (CD45⁺, P2RY12/CD68⁺, CD49D) and MDM (CD45⁺, P2RY12/CD68⁺, CD49D⁺) and vessels (CD31⁺) in *IDH* WT glioma. Dashed line indicates the border of the perivascular niche (PVN), scale bar represents 100μm. (B) Heatmap of cell-type gene set variation analysis (GSVA) enrichment scores of micro-dissected Ivy Glioblastoma Atlas Project samples (dataset from Puchalski et al., 2018). Columns are ordered by anatomical location, rows have been z-scored. (C) Gene set enrichment analysis (GSEA) results of MSigDB "C2" antigen processing and cross-presentation associated pathways in T-MDMs versus T-MG in *IDH* WT glioma. (D) Heatmap of MDM *IDH* WT gene set expression in sorted MG and MDMs from *IDH* mut and WT glioma samples. Columns are ordered by *IDH* status and cell type, expression values have been z-scored. (E) Plot of z-scored MDM *IDH* WT signature scores in the TCGA glioma dataset. Subjects are ranked by their enrichment score (small amount of random variation added for readability) and the *IDH* status is indicated by color. (F) Kaplan-Meier estimator of survival in the combined TCGA glioma cohort based on the enrichment for a cell type-specific T-MDM signature (see Figure S2E). (G) ORA of "innate anti-PD-1 resistance" (IPRES) signatures within DEG from MG- and MDMs in *IDH* WT gliomas DEGs (versus MG from *IDH* mut tumors) with tile fill indicating the -log10 of the adjusted p value. (H) GSVA of IPRES signatures in CD45⁻ cells, MG, and MDMs from *IDH* mut and *IDH* WT gliomas. Columns are ordered by cell type, rows (z-score) have been hierarchically clustered.
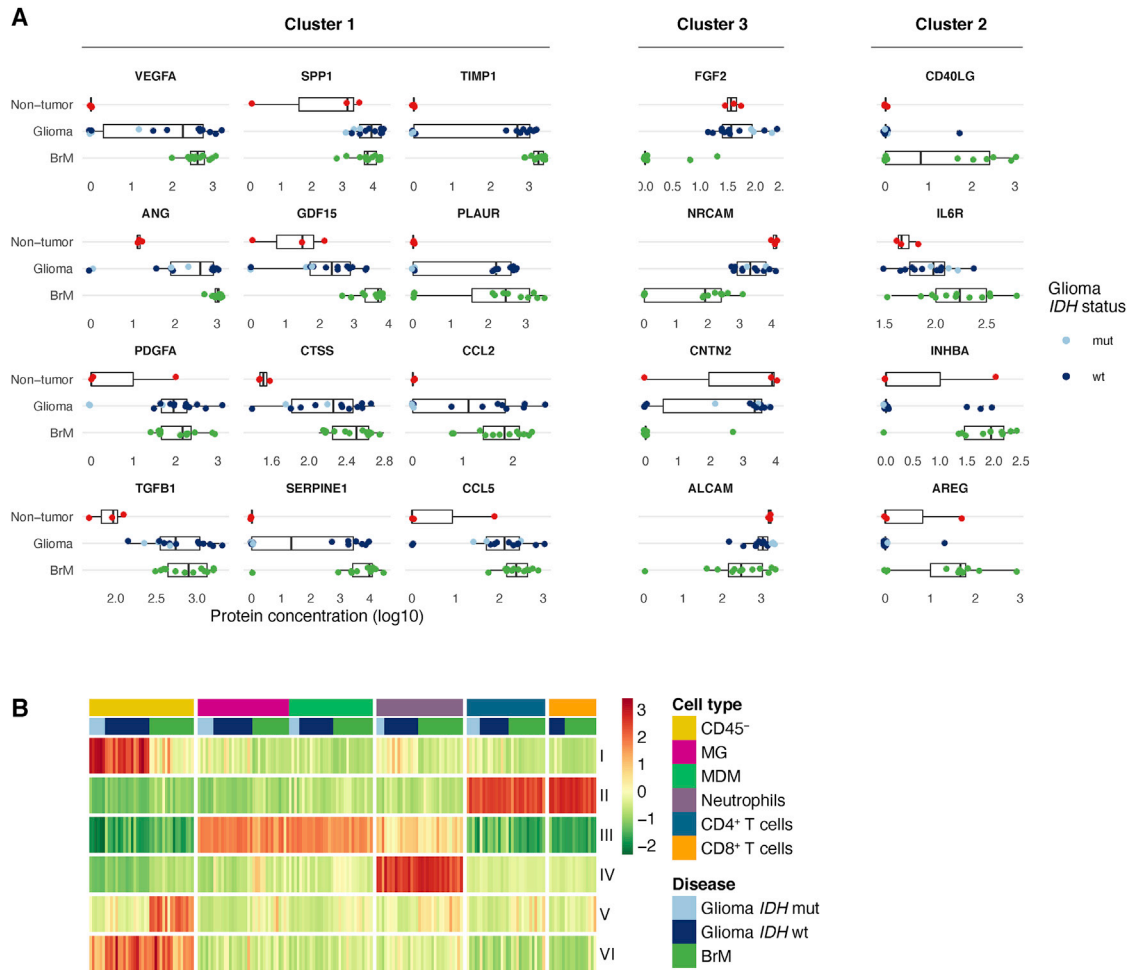
Figure S5. Protein Concentration in Bulk Tumor Tissues and Relation to Cell-Type-Associated SOM Spots, Related to Figure 5

(A) Bulk tissue protein concentrations of indicated proteins in non-tumor brain (n = 3), gliomas (n = 14) and BrMs (n = 12). Color indicates disease type and *IDH* status. (B) Heatmap of self-organizing map (SOM) spot metagene expression across the analyzed samples. Rows were z-scored and have been hierarchically clustered, columns were ordered by cell type, disease type and *IDH* mutation status.

A MG

BrM
vs
IDH wt Glioma

291

531

117

447

IDH wt Glioma
vs
Non-tumor

BrM
vs
Non-tumor

742

576

B MDM

BrM
vs
IDH wt Glioma

131

128 / 32

IDH wt Glioma
vs
in vitro

BrM vs
in vitro

338

1639

589

C

BrM-MG vs. BrM-MDM
"Biocarta IL6 pathway"
NES=1.62, p-adjust=0.09

D

BrM-MDM vs. BrM-MG
"Naba core matrisome"
NES=2.22, p-adjust=0.02

E

CXCR1 *CXCR2* *CXCL1* *CXCL2* *CXCL5* *CXCL8*

CXCR4 *CXCL12*

Disease
■ Glioma *IDH* wt
■ BrM
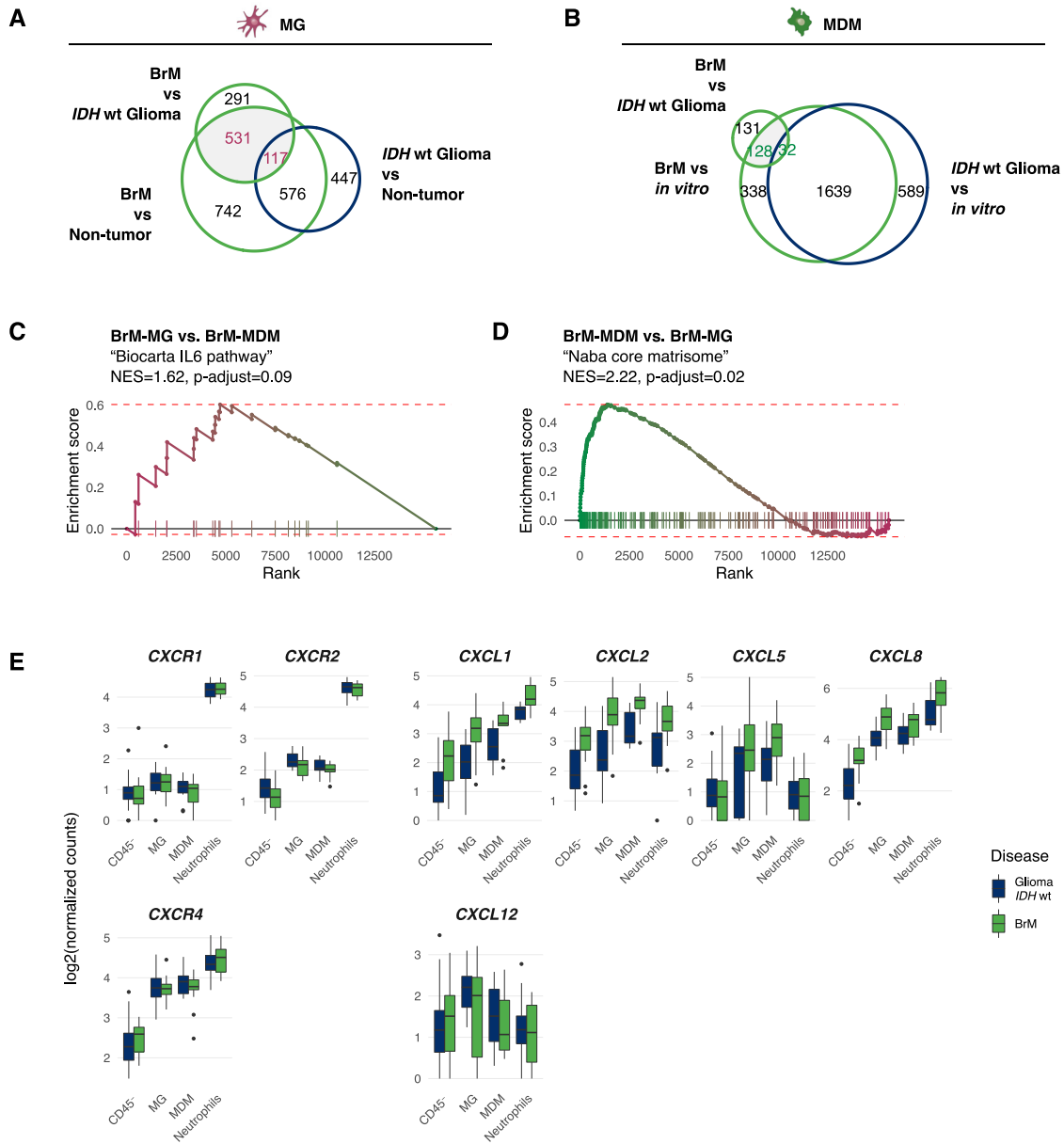
Figure S6. Gene Expression Analysis in BrM-TAMs, Related to Figure 6

(A) Overlap of the number of differentially expressed genes (DEG, log2(fc) > 1, p.adj < 0.05) in MG and (B) MDMs in the indicated comparisons. BrM-specific gene sets are highlighted in gray within each cell type. The intersect of highlighted BrM-MG and BrM-MDM sets contains 87 genes. (C) GSEA of the "Biocarta IL-6 pathway" in BrM-MG versus -MDM and the (D) "Naba core matrisome" gene set from the MSigDB "C2" collection in BrM-MDM versus -MG. (E) Expression (log10-transformed normalized counts) of neutrophil-recruiting chemokines and receptors in sorted MG, MDMs and neutrophil populations from *IDH* WT and BrM samples.

A **Immunofluorescence**

Glioma *IDH* wt

DAPI CD45 CD68/P2RY12 CD49D CD3

BrM

DAPI CD45 CD68/P2RY12 CD49D CD3

B

	greenyellow	lightcyan	lightyellow	magenta	brown	salmon	blue	grey60	tan	pink	cyan	midnightblue	purple	turquoise	yellow	
	0.2	0.9	0.2	0.4	2e-04	2e-05	0.09	4e-09	7e-05	0.9	0.09	8e-04	0.001	3e-04	0.002	TAM Glioma *IDH* wt
	0.2	0.9	0.2	0.4	2e-04	2e-05	0.09	4e-09	7e-05	0.9	0.09	8e-04	0.001	3e-04	0.002	TAM BrM
	0.1	0.8	0.01	0.4	0.8	0.1	0.4	7e-04	0.003	0.02	0.8	0.1	0.2	0.7	0.2	MG BrM
	1	1	0.4	0.1	8e-05	0.002	0.005	0.005	0.1	0.04	0.1	0.02	0.02	2e-04	0.02	MDM BrM
	0.03	0.3	0.2	0.4	0.03	0.06	0.7	0.02	0.06	0.1	0.01	0.3	0.07	0.1	0.01	CD4+ %CD45+
	0.05	0.02	0.07	0.05	0.7	0.3	0.7	0.03	0.4	0.2	0.5	0.02	0.2	0.4	0.8	CD8+ %CD45+

0.6
0.4
0.2
0
−0.2
−0.4
−0.6

C BrM MDM-module: "brown"

NABA ECM AFFILIATED

REACTOME IMMUNOREGULATORY INTERACTIONS BETWEEN A LYMPHOID AND A NON LYMPHOID CELL

REACTOME O LINKED GLYCOSYLATION OF MUCINS

PID INTEGRIN A9B1 PATHWAY

REACTOME CELL SURFACE INTERACTIONS AT THE VASCULAR WALL

KEGG NOD LIKE RECEPTOR SIGNALING PATHWAY

REACTOME NUCLEOTIDE BINDING DOMAIN LEUCINE RICH REPEAT CONTAINING RECEPTOR NLR SIGNALING PATHWAYS

REACTOME DEGRADATION OF THE EXTRACELLULAR MATRIX

REACTOME HEMOSTASIS

REACTOME INNATE IMMUNE SYSTEM

REACTOME TRANSMEMBRANE TRANSPORT OF SMALL MOLECULES

REACTOME RESPONSE TO ELEVATED PLATELET CYTOSOLIC CA2

REACTOME PLATELET ACTIVATION SIGNALING AND AGGREGATION

REACTOME TRANSPORT OF GLUCOSE AND OTHER SUGARS, BILE SALTS AND ORGANIC ACIDS METAL IONS AND AMINE COMPOUNDS

REACTOME SLC MEDIATED TRANSMEMBRANE TRANSPORT

REACTOME CELL CELL COMMUNICATION

-log10(p)

2
6
10

REACTOME G ALPHA I SIGNALLING EVENTS

REACTOME CHEMOKINE RECEPTORS BIND CHEMOKINES

REACTOME CYTOSOLIC SULFONATION OF SMALL MOLECULES

REACTOME CLASS A1 RHODOPSIN LIKE RECEPTORS

NABA SECRETED FACTORS

KEGG HEMATOPOIETIC CELL LINEAGE

REACTOME SIGNALING BY GPCR

REACTOME GPCR LIGAND BINDING

REACTOME GPCR DOWNSTREAM SIGNALING

KEGG CHEMOKINE SIGNALING PATHWAY

KEGG CYTOKINE CYTOKINE RECEPTOR INTERACTION

REACTOME SIGNALING BY ILS

REACTOME CYTOKINE SIGNALING IN IMMUNE SYSTEM

PID IL2 1PATHWAY

Figure S7. Correlation of WGCNA Modules with External Traits and Module Pathway ORA, Related to Figure 7

(A) Representative immunofluorescence images in *IDH* WT gliomas and BrMs. Scale bars = 100μm, boxed area is shown in higher magnification in Figure 7A. (B) Heatmap of the weighted gene correlation network analysis (WGCNA) module eigengene (= first principal component of expression data, columns, module columns are labeled with a color code) correlation to the traits (rows, cell type and disease, abundance of CD4+ or CD8+ T cells in % of CD45+). Values inside the cells state Pearson's r and the associated p value. (C) "Brown" BrM-MDM module MSigDB "C2CP" ORA results (p value < 0.01) enrichment map network visualization. Node size represents p value, edge thickness reflects overlap of genes between gene sets.